ESCUELA POLITÉCNICA SUPERIOR

DEPARTAMENTO DE BIOINGENIERÍA E INGENIERÍA AEROESPACIAL

PROYECTO FIN DE CARRERA

CALIBRATION OF A C-ARM X-RAY SYSTEM FOR ITS USE IN TOMOGRAPHY

Autor:
Martín Paraíso Labora

Tutor:
Mónica Abella García

Leganés, febrero de 2013.

Título: Calibration of a C-arm X-ray system for its use in tomography

Realización: Departamento de Bioingeniería e Ingeniería Aeroespacial / Laboratorio de Imagen Médica, Unidad de Medicina y Cirugía Experimental. Hospital General Universitario Gregorio Marañón.

Autor: Martín Paraíso Labora.

Director: Mónica Abella García.

EL TRIBUNAL

Presidente: _____

Vocal: _____

Secretario: _____

Realizado el acto de defensa y lectura del Proyecto Fin de Carrera el día __ de _____ de 20__ en Leganés, en la Escuela Politécnica Superior de la Universidad Carlos III de Madrid, acuerda otorgarle la CALIFICACIÓN de

VOCAL

SECRETARIO PRESIDENTE

ACKNOWLEDGEMENT

Gracias a Manolo y a Juanjo por darme la oportunidad de realizar mi proyecto fin de carrera en el LIM y por su aportación a la investigación biomédica.

Quiero agradecer a mi tutora, Mónica, todo el esfuerzo realizado para que este proyecto se haya realizado. He aprendido mucho de tu capacidad de trabajo y de tu tesón. Te deseo lo mejor. Estoy seguro de que llegarás muy lejos en la investigación y espero que la universidad y tus alumnos aprovechen al máximo tu sabiduría.

Debo nombrar, por obligación divina, a Claudia, grandísima amiga que siempre ha estado allí para ayudarme con cualquier problema. De la misma manera a Aurora, otra magnífica persona, estupenda amiga y mejor compañera de trabajo que tampoco ha dudado a la hora de ayudarme. A Carlos, al que quiero mucho. Y a Juanjo, a quien también quiero mucho. Juntos nos hemos divertido muchísimo y hemos pasado momentos inolvidables. A vosotros va dedicado este proyecto.

También está dedicado de manera especial a Carmen, por su fuerza y alegría, y el gran apoyo que es para todos nosotros.

Muchas gracias a mi amigo Subhra, por su enorme ayuda y generosidad y a los compañeros de la UPM.

Agradezco profundamente a todos los miembros del LIM vuestra ayuda y vuestra alegría. Para mí es un orgullo haber trabajado junto a vosotros. Sois todos muy sabios y trabajáis por una causa magnífica. Ver a gente como vosotros trabajando en investigación me llena de alegría y optimismo.

Ha sido un honor formar parte de este grupo y haber aportado mi pequeña parte.

:)

ABSTRACT

Intraoperative radiotherapy (IORT) is a procedure that allows the administration of a high dose of ionizing radiation directly on the tumor bed just after the surgery. The main advantage with respect to external radiotherapy (RT) is that it allows exposing the tumor bed at maximum avoiding radiation on surrounding healthy tissue.

The first tool for IORT planning was developed by GMV in collaboration with the imaging group at Gregorio Marañón Hospital inside a line of research devoted to IORT. The tool was based on a previous CT image as it is done for external radiotherapy planning. The problem in the case of IORT lies in the changes suffered by the patient's anatomy during surgery and after resecting the tumor, making the dose calculations imprecise, as they were done based on CT images previous to the intervention. Within this line of research, obtaining volumetric images of the patient during the intervention using a C-arm as a tomograph has been proposed to evaluate and/or improve the results on IORT planning.

A C-arm is a portable system with a wide variety of movements that allows obtaining projective images (radiographies) from multiple perspectives of the operating table during an intervention, avoiding the need of moving the patient. For the development of this project a C-arm by SIEMENS (model: Siremobil Compact L) is available.

In order to use the system, designed originally to obtain planar images, as a tomograph, it is necessary to make an evaluation of the possible non-idealities (distortion in the detector, repeatability and geometrical misalignments) and its effects on the reconstructed images. Furthermore, it is necessary to develop a calibration algorithm that allows obtaining the correction value to compensate them in reconstruction. The objective of this thesis is to give answers to these two needs.

In the first place, the evaluation of the projection images has been done by making a distortion and repeatability study based on acquisitions of different phantoms. Secondly, the effects of geometrical misalignments on both projections and reconstructions have been evaluated. To this end, a software tool has been developed to emulate the acquisition done by the C-arm, producing a set of projections of synthetic phantoms based on the parameters that describe the real system. This tool allows modeling the geometrical misalignments applying inclinations, rotations and translations on the detector and changes on the value of source-to-detector distance.

Finally a software calibration tool has been developed, based on the method proposed by Cho et al. in 2005, an algorithm specifically designed for its use with a C-arm. It allows the estimation of a set of parameters that describe the system geometry. With these parameters, the reconstruction algorithm can compensate the non-idealities to obtain a good quality reconstruction.

KEY WORDS

X-ray Computed Tomography (CT), C-arm, Intraoperative Radiotherapy (IORT), cone-beam geometry, artifact, misalignment, geometrical calibration.

RESUMEN

La radioterapia intraoperatoria (RIO) es un procedimiento que permite la administración de una alta dosis de radiación ionizante directamente sobre el lecho tumoral justo después de la intervención quirúrgica. La principal ventaja con respeto a la radioterapia externa (RT) externa es que permite exponer el tejido tumoral al máximo evitando radiar tejido sano circundante.

La primera herramienta de planificación de RIO fue desarrollada en el Laboratorio de Imagen Médica de la Unidad de Medicina y Cirugía Experimental del Hospital General Gregorio Marañón y el Departamento de Bioingeniería de la Universidad Carlos III de Madrid dentro de la línea de investigación en RIO. La herramienta se basa en una imagen previa de TAC al igual que se hace en la planificación en radioterapia externa. El problema en el caso de la RIO radica en que la anatomía del paciente sufre cambios durante la cirugía y tras la extirpación del tumor, haciendo imprecisos los cálculos hechos basándose en una imagen de TAC previa a la intervención. Dentro de esta línea de investigación, para valorar y/o mejorar los resultados de la planificación, se ha propuesto obtener imagen volumétrica del paciente durante la intervención usando un arco en C como tomógrafo.

El arco en C es un equipo portátil con amplia variedad de movimientos que permite la toma de imágenes proyectivas (radiografías) desde múltiples perspectivas en la mesa de cirugía durante una intervención, evitando la necesidad de trasladar al paciente. Para la realización de este proyecto se dispuso de una arco en C de SIEMENS (modelo Siremobil Compact L).

Para poder utilizar este sistema, diseñado originalmente para obtener imagen plana, como tomógrafo es necesario hacer una evaluación de las posibles no-idealidades (distorsión en el detector, repetitividad y desalineamientos geométricos) y su efecto en las imágenes reconstruidas. Así mismo, es necesario desarrollar un algoritmo de calibración que permita obtener el valor de corrección que permita compensarlas en la reconstrucción. El objetivo de este proyecto es dar respuesta a estas dos necesidades.

En primer lugar se ha realizado la evaluación de las imágenes de proyección haciendo un estudio de distorsión y repetitividad a partir de adquisiciones de diferentes maniquíes. En segundo lugar, se han evaluado los efectos de los desalineamientos geométricos tanto en las proyecciones como en las imágenes reconstruidas. Para ello se ha desarrollado una herramienta software que emula la adquisición que realiza el arco, produciendo un conjunto de proyecciones a partir de maniquíes sintéticos basándose en los parámetros que describen el sistema real. Esta herramienta permite modelar desalineamientos geométricos aplicando inclinaciones, rotaciones y traslaciones en el detector, y cambios en el valor de la distancia fuente-detector.

Finalmente se ha desarrollado una herramienta software de calibración, basada en el método propuesto por Cho et al en 2005, un algoritmo específicamente diseñado para su utilización con un arco en C que permite estimar un conjunto de parámetros que describen la geometría del sistema. A partir de estos parámetros el algoritmo de reconstrucción compensa las no-idealidades para conseguir una reconstrucción de calidad.

PALABRAS CLAVE

Tomografía computerizada de rayos X (CT), arco en C, Radioterapia Intraoperatoria (RIO), geometría *cone-beam,* artefacto, desalineamiento, calibración geométrica.

INDEX OF CONTENTS

FIGURE LIST

1. INTRODUCTION

1.1. Introduction to X-rays

Wilhelm C. Roentgen discovered the X-rays by chance while working with a cathode ray tube in November 1895.

X-rays are a type of high-energy electromagnetic radiation and are therefore usually explained by the theory of corpuscle, in other words, as a particle or photon. The energy of an X-ray photon is defined as follows:

$$E = \frac{h \cdot c}{\lambda}$$

where $h = 4{,}135 \cdot 10^{-15}$ is Planck constant, c is the speed of light, λ is photon wavelength and ν is the frequency. Figure 1-1 illustrates the electromagnetic spectrum in terms of frequency, wavelength and energy. In medical imaging, X-ray photons of energies between 10 keV and 150 keV are used (Beutel et al. 2000). When working with X-rays between 10 eV and 30 keV, are called "soft" and are used in microscopy.

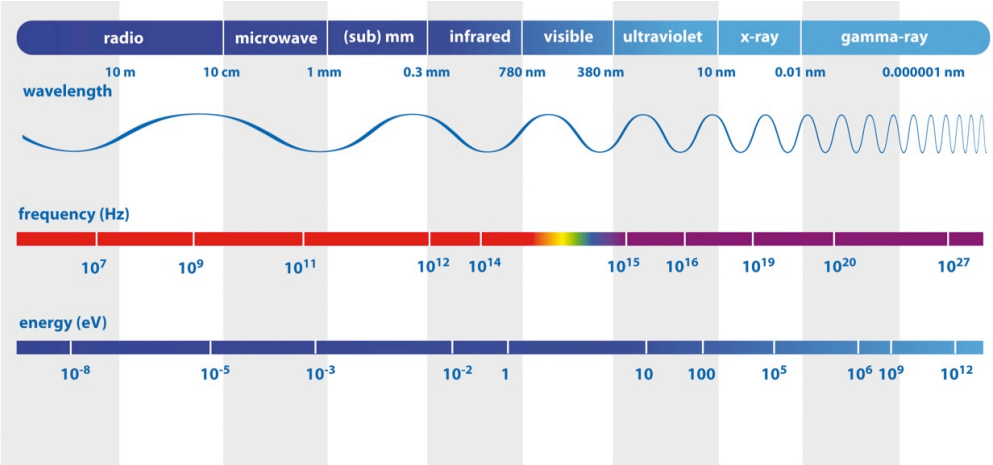

Figure 1-1. Electromagnetic spectrum and X-ray position.

X-rays are ionizing radiation since their high energy is enough to strip off electrons from the atoms. Exposure to such radiation can cause the rupture of some molecules and induce chemical reactions in the organism, especially important in the case of water molecules due to the generation of free radicals, which are very reactive.

1.1.1. Generation of X-rays

The X-rays are produced by the partial conversion of the kinetic energy of highly accelerated electrons into X-ray photons (Jan 2006). Inside the X-ray tube (vacuum-sealed), a filament (cathode) is heated in order to emit a cloud of electrons that are accelerated by high voltage applied between the cathode and the anode (Figure 1-2). These electrons impact the anode (usually tungsten) and giving out their kinetic energy mainly as heat and only a 4% as X-ray photons. Figure 1-3 shows two examples of X-ray sources. In the right panel we can see a shielding usually made of lead to prevent the X-rays to go in all directions.

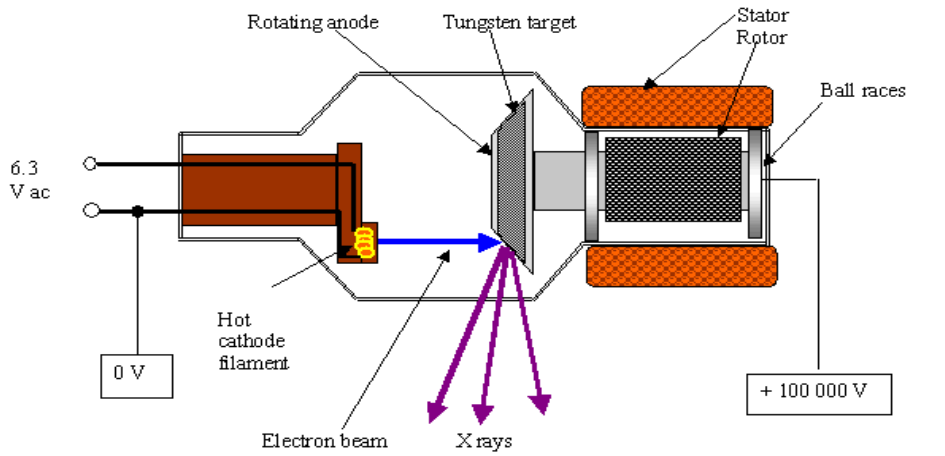

Figure 1-2 Sketch of an X-ray tube.

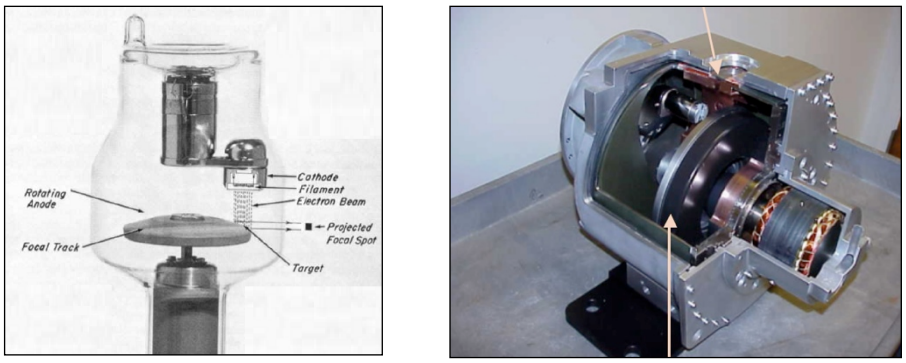

Figure 1-3 Primitive X-ray tube example (left) and actual X-ray tube (with shielding) (right).

X-ray photon generation can be achieved by two different phenomena:

- **Braking radiation (*Bremsstrahlung*)**: it is produced when an electron passing near the atom nucleus of the anode is decelerated (braking) changing its trajectory and releasing part of its kinetic energy in the form of X-ray photon. The number of photons obtained by this phenomenon is inversely proportional to their energy as seen in Figure 1-5.

- **Characteristic radiation:** this type of radiation is produced when an electron ionizes one of the atoms of the anode extracting an electron from an inner layer (layer *K* in Figure 1-4). To fill the gap, an electron from an outer layer jumps to the inner layer releasing its excess of energy (de-excitation) in the form of an X-ray photon. This photon will have an energy equal to the energetic difference between the two layers (characteristic energy). Figure 1-5 shows peaks on characteristic radiation, representing the characteristic energy photons generated. If, however, the electron (incident) extracts an electron from one of the outer layers, the de-excitation will result in the release of lower energy photons (e.g. ultraviolet light).

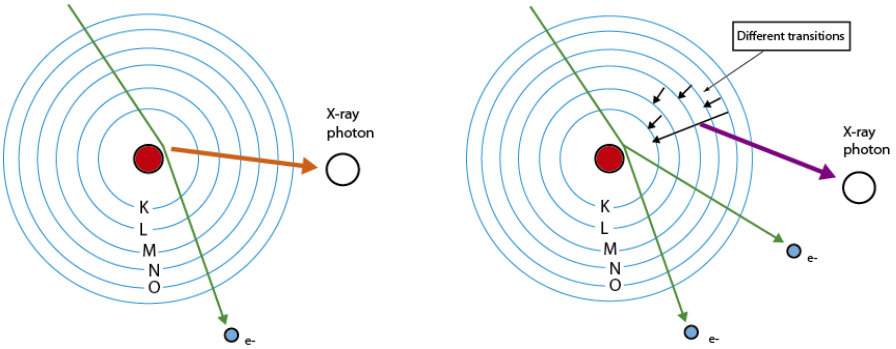

Figure 1-4 Sketch of the processes involved in the generation of X-rays: Bremsstrahlung (left) and characteristic radiation (right).

Most of the low energy photons are absorbed within the X-ray tube, affecting to the spectral distribution at low energies in Figure 1-5.

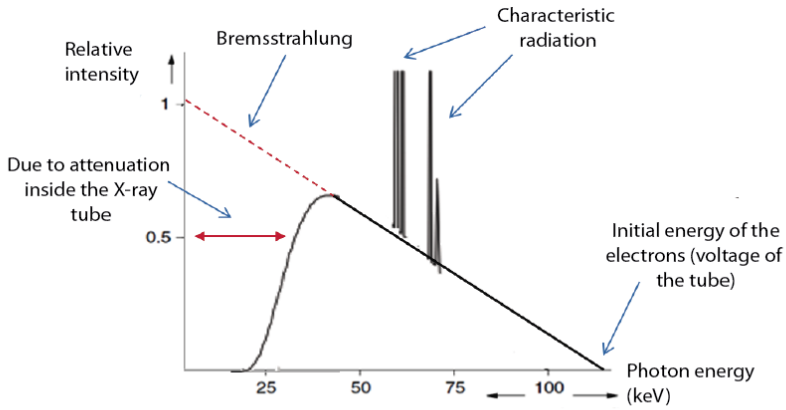

Figure 1-5 Characteristic form of the X-ray emission spectrum due to the typical phenomena that occur in the X-ray tube. Source: (Beutel et al. 2000).

1.1.2.X-ray interaction with matter

In the energy spectrum commonly used in radiology (10-150 KeV), the X-ray photon interaction with matter is either one of three effects: *Rayleigh, Compton* and photoelectric (Figure 1-6).

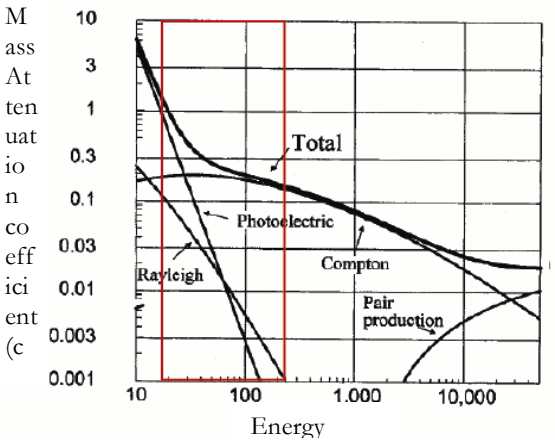

Figure 1-6 Diagram of the different phenomena produced by the interacting X-ray photons with soft tissue (photoelectric effect, *Compton*, *Rayleigh* and pair production) as a function of the energy of these

photons. The red box shows the energy range (keV) used in medical imaging where photoelectric effect, *Rayleigh and Compton* are present. (Source: scientificsentence.net).

These processes occur due to the following phenomena (see Figure 1-7 for illustrations):

- **Photoelectric effect** occurs when an X-ray photon gives off its energy to an electron as kinetic energy pushing it off the atom (ionization).

- ***Compton* effect** is produced when an X-ray photon collides with an electron orbiting the atom, creating a lower energy photon with a different trajectory depending on the initial energy and the angle of incidence.

- ***Rayleigh* effect** is scattering process. It is produced when the incident X-ray photon interacts with the electric field of an electron orbiting the atom. The photon is scattered without interacting with the atom inner structure. There is no energy variation.

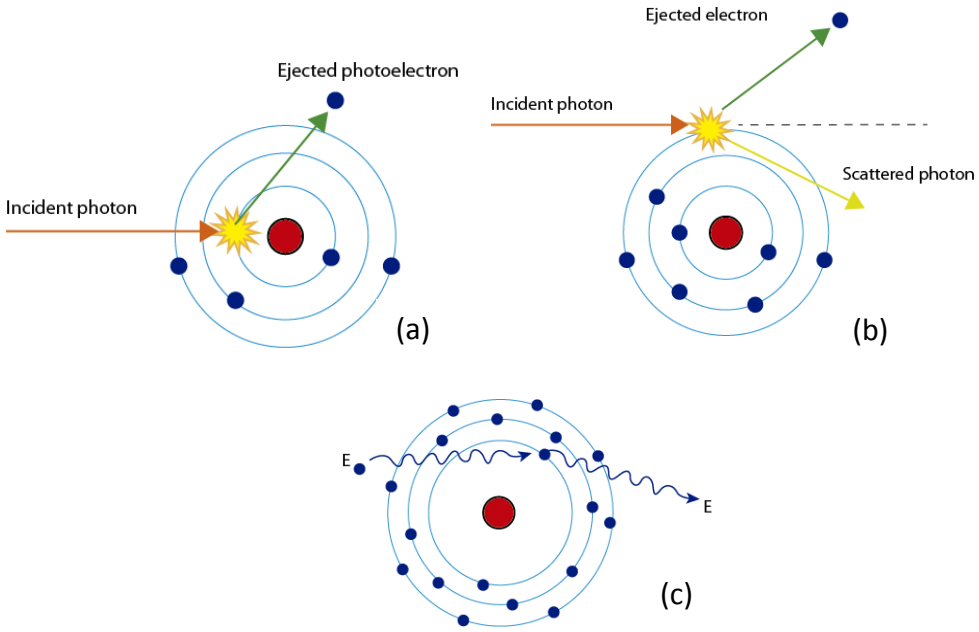

Figure 1-7 Diagrams of the processes that occur when X-ray photons interact with matter: (a) Photoelectric effect, (b) Compton effect and (c) Rayleigh effect.

1.1.3.X-ray detection

The first X-ray detectors used in medicine were based on photographic film covered by a silver emulsion. The film is more sensitive to light photons than to X-rays, so high doses are required to obtain an image with reasonable quality. Because of this problem, intensifying screens were introduced, placed in contact with the photographic film (Figure 1-8). When X-rays interact with the fluorescent screen, light photons are released to excite the photographic film. This reduces the amount of radiation needed to obtain a good quality image, decreasing X-ray dose to the patient.

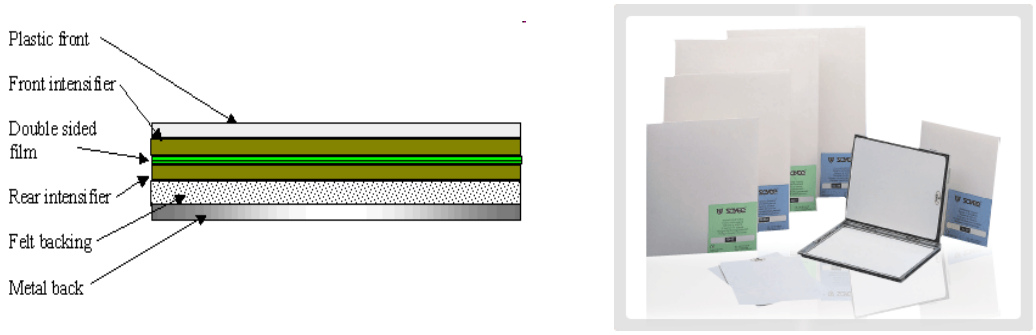

Figure 1-8 Cross section representation of a film covered on both sides by a fluorescent screen (left) and (right) example of commercial intensifier screen by Soyee Product Inc. (right).

Later in the 80's, the first digital systems known as CR (Computed Radiography) appeared. These systems generate the digital image in two steps. First, the X-ray photons excite electrons in a phosphor crystal layer, which implies the temporary storage of their energy. Secondly in the reading step, the crystal layer is excited with a laser, allowing the stored energy to be released as visible light. Finally, the light is collected in a photomultiplier array and amplified turning into electrical signal (analog). In the last step, analog/digital conversion is performed. The complete process is outlined in Figure 1-9.

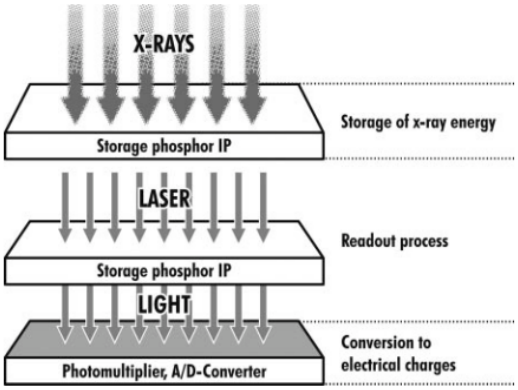

Figure 1-9 Composition diagram of a CR digital detection system. Source: (Körner et al. 2007).

Reading and conversion occurs in specific systems outside the X-ray catchment system. The incorporation of CR in the clinical radiography room is simple since it only requires the exchange of the photographic plate for the new detector panel in the same rack, as shown in Figure 1-10.

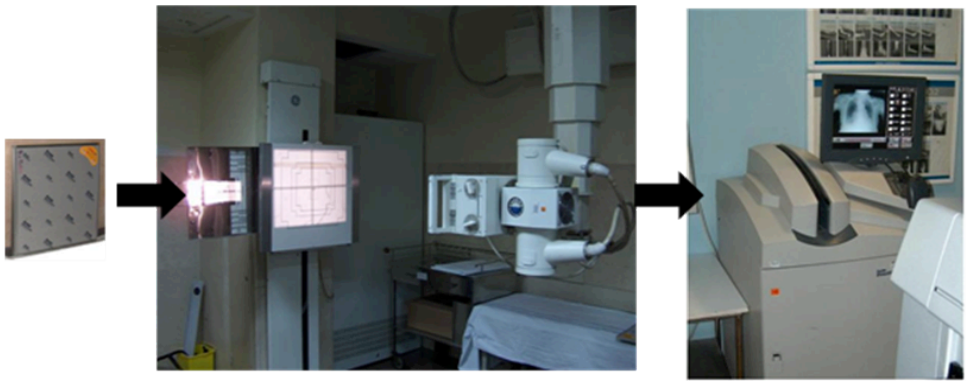

Figure 1-10 Example of CR clinical system with the acquisition system and the case, which is inserted into the same slot that the photographic film (left) and the CR (scanner) where data is read (right).

Later in 1990, the first DR (Direct Radiography) systems appeared. These systems convert X-rays directly into digital signals avoiding the reading stage of CR systems.

DR systems are divided into direct and indirect depending on the type of X-ray conversion (Figure 1-11). In direct conversion systems X-ray photons are converted into electrical signals in a single step through a photoconductor layer. In indirect conversion (e.g. flat panel detectors), X-ray photons are first converted into visible light proportionally to the detected photons and then these light photons are converted into electrical charges by a photodiode array. Besides its small size, it offers the best image quality and best performance in low contrast of all digital detectors. The disadvantage is the higher cost.

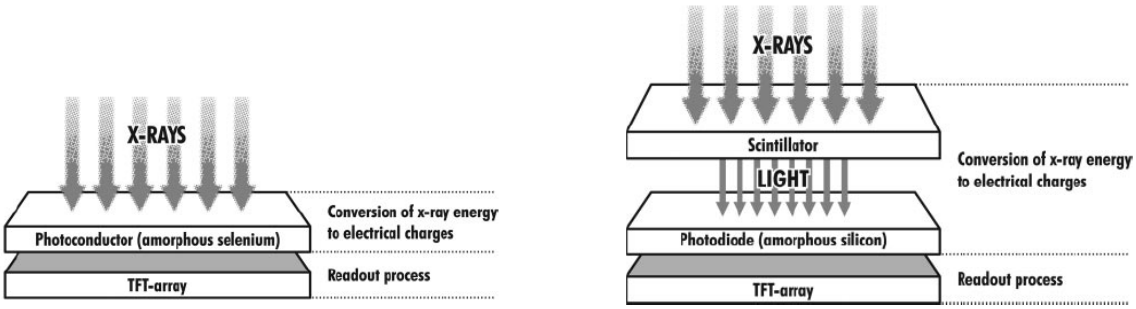

Figure 1-11 (Left) Composition diagram of a direct conversion DR digital detection system and (right) composition diagram of an indirect conversion DR digital detection (flat panel). Source: (Körner et al. 2007).

1.2. X-ray tomography systems

Tomography, from the Greek *tomé* (cut) and *grafos* (drawing) is, in general terms, the technique that allows obtaining images of the slices of an object without actually performing any cut. There are different types of tomographic systems:

- First systems had a source and a 1-element detector moving in parallel with small increments to fill in one projection line. Then the pair source-detector rotated around the object under study to obtain a new projection line in different projection angles. The process is shown in Figure 1-12, where all X-rays paths for one projection line are parallel corresponding with the so-called **parallel-beam** geometry.

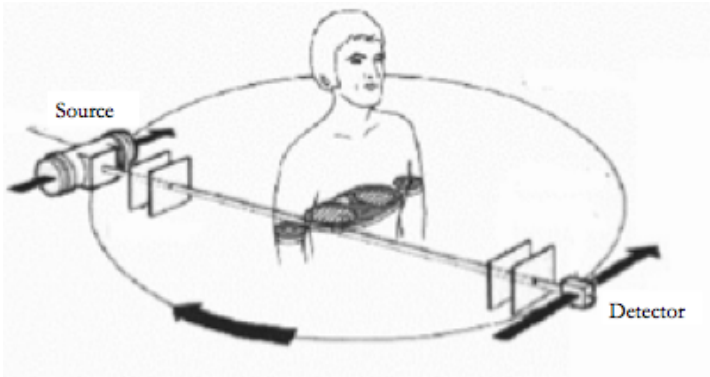

Figure 1-12 Illustration of a primitive tomograph with acquisition based on parallel-beam geometry.

- In order to make a good use of the radiation emitted by the tube in directions different from the perpendicular to a certain plane and reduce the number of displacements of source and detector, the 1-element detector evolved into a line of detector elements. In this type of systems the paths described by the rays are not parallel anymore, but diverge from the same point forming the shape of a fan (Figure 1-13). For this reason this is known as **fan beam** geometry.

  Attending to the shape of the detector, we can find two different configurations:
  - Equispaced rays, where detector follows a straight line.
  - Equiangular rays, in which the detector forms an arc.

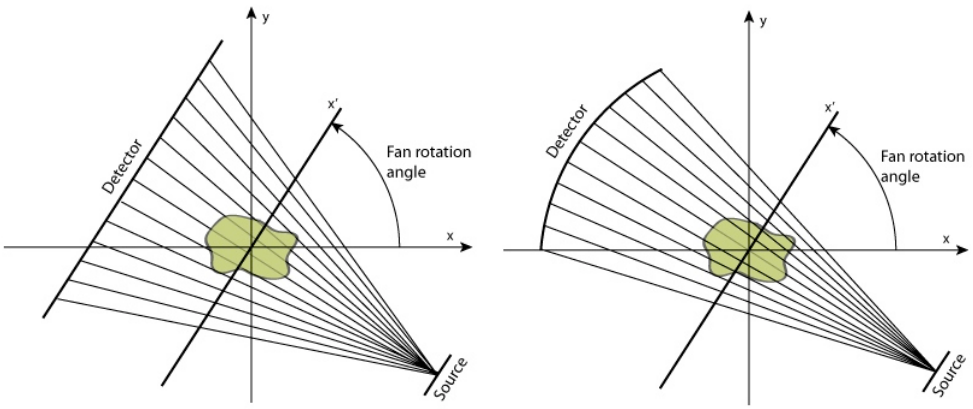

Figure 1-13 Second generation tomographs, with fan-beam geometry: equispaced rays (left) and equiangular rays (right) models.

- The idea of fan-beam was extended to three dimensions in order to have faster acquisitions. Using the rays emitted in all directions the detector became a plane. In these systems, rays pass through the body forming a cone, following the geometry known as **cone-beam** (Figure 1-14).

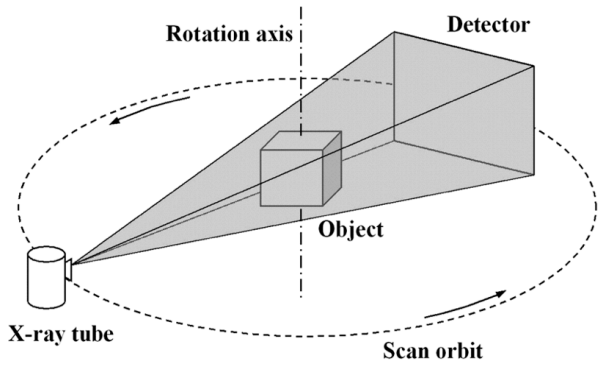

Figure 1-14 Diagram of acquisition in a cone beam geometry tomograph.

- Finally, fan beam and cone beam concepts were extended into a spiral. In helicoidal systems, source and detector rotate around the patient while the bed is moved longitudinally. Therefore, rays describe a spiral or **helicoidal** path regarding to patient (Figure 1-15).

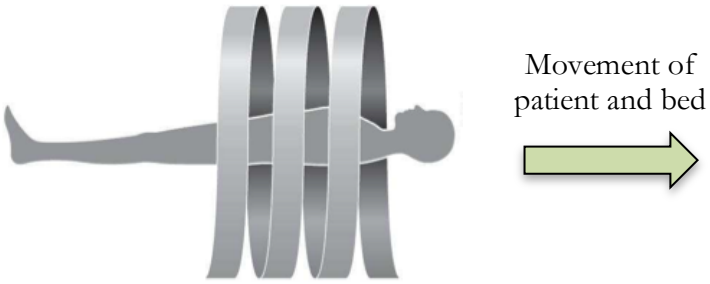

Figure 1-15 Illustration of a cone beam geometry tomograph acquisition.

1.2.1.Projection

The data obtained by an X-ray detector is what we know as projections. To get an intuitive idea of what projection is, we will start with a simple example of a 2D image with different attenuation coefficients (different μ values) and parallel ray geometry (Figure 1-16). The projection for angle $\theta = 0^{\circ}$ will be the sum of attenuation coefficients through the horizontal trajectory of each ray. The total attenuation suffered by each ray is represented in the projection data where the *t* axis shows the distance from the ray to the object's coordinate center. Nevertheless, this information is not enough to know the disposition and values of attenuation of the whole object. If a new projection is taken for $\theta = 90^{\circ}$, we will also have information of the total attenuation through the vertical axis. In this simple case (without noise) just two rays for two different angles are required in order to obtain a 4-equation/4-unknown system. For a real case, the number of unknowns is greater so more projections will be needed to be able to reconstruct the object in a scanner.

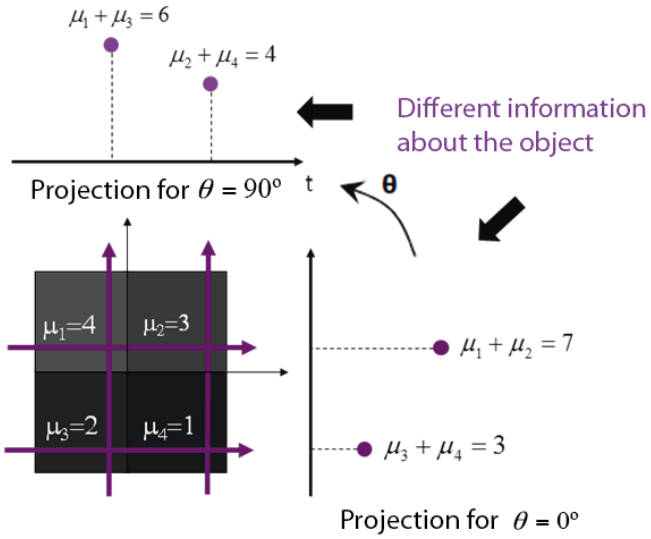

Figure 1-16 Simple example for projection.

Formal definition of projection

When extending the previous example to continuous case, each projection is a set of line integrals of some property of the image as it is defined in the following equation for parallel rays case (Figure 1-17):

$$P_\theta(t) = \int_{(\theta,t)} f(x,y)\cdot ds = \int_{-\infty}^{\infty} f(x,y)\cdot \delta(x\cdot\cos(\theta) + y\cdot sen(\theta) - t)\cdot dx\cdot dy$$

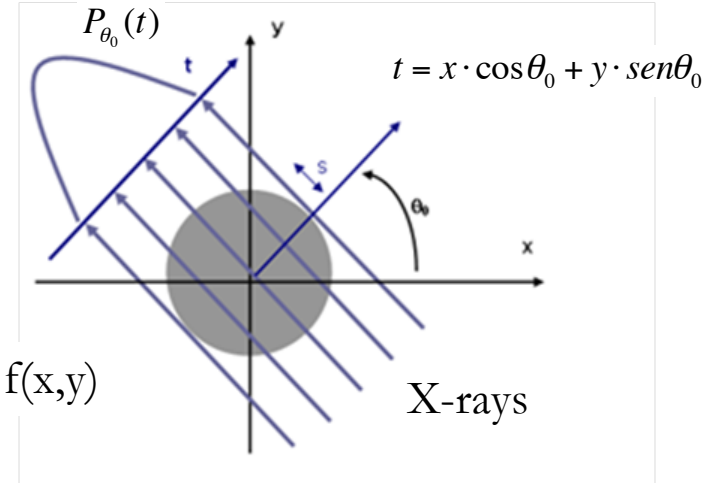

Figure 1-17 Sketch of projection. Lines represent parallel rays that go through the object f(x,y) for projection angle θ_0 and integrals along each line represent the projection value for this angle, $P_{\theta_0}(t)$. We can see that projection values are higher in the center and lower at sides because central rays are the ones that traverse a bigger part of the object.

For the case with parallel rays (known as parallel-beam geometry), the $P_\theta(t)$ function defined for every *t* and θ values is known as *Radon* transform of $f(x,y)$ function.

1.2.2. Reconstruction: Methods

The aim in tomography is to reconstruct a 3D volume based on projection data (line integrals). A variety of reconstruction methods exist, which can be grouped in analytic methods and iterative methods depending of the mathematical base used for the inversion when going from the projections to the original data set.

1.2.2.1. Analytical reconstruction methods

These methods are based on the discretization of an idealized mathematical model in the continuous space. They assume that the projections are line integrals of the volume to reconstruct. A set of parallel line integrals constitutes the Radon Transform, P_θ :

$$P_\theta(t) = \int_{(\theta,t)} f(x,y)ds = \int_{-\infty}^{\infty} f(x,y)\delta(x\cdot cos\theta + y\cdot sen\theta - t)dxdy$$

The central slice theorem is the basis of the Radon Transform inversion. The theorem states that "*Fourier transform of a parallel projection of a f(x,y) distribution for a* θ *angle, is equal to the values of the 2D Fourier transform of a distribution in the line passing through the origin and forming the same* θ *angle with u axis"* (Kak 1988). Figure 1-18 illustrates the central slice theorem.

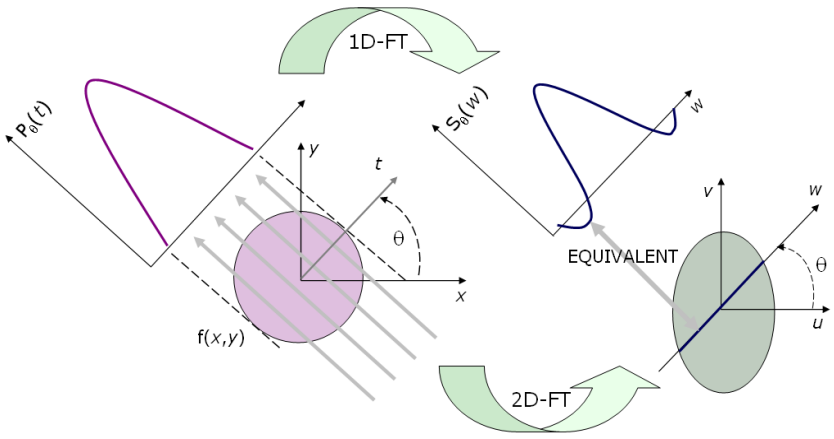

Figure 1-18 Central slice theorem. Source: (Abella 2010).

From this theorem, two types of approximation are proposed to invert the *Radon* transform to obtain *f(x,y)*: the ones based on the Fourier inverse transform and the ones based on filtered backprojection.

1.2.2.2. Fourier Direct Method

Making use of the central slice theorem, calculating the 1D Fourier transform of the projections at different angles of a certain object, f(x,y)$\mathrm{f(x,y)}$, it is possible to determine the values in the 2D Fourier transform in the object, *F(u,v)*. If infinite number of projections were taken, every point in *F(u,v)* would be known and therefore, $\mathrm{f(x,y)}$ could be recovered exactly using the Fourier inverse transform:

$$f(x,y) = \iint_{-\infty}^{\infty} F(u,v) \cdot e^{j2\pi(ux+vy)} du dv$$

In practice, only a finite set of projections is available and the function $F(u, v)$ is only known along a finite number of radial lines. In order to be able to use the *FFT (Fast Fourier Transform),* one must then interpolate from these radial points to the points on a square grid as indicated in the middle panel of Figure 1-19. This step is the most delicate one in these methods: since the density of the radial points becomes sparser as one gets farther away from the center, the interpolation error also becomes larger. This implies that there is a higher error in the calculation of the high frequency components of an image than in the low frequency ones, which results in some image degradation.

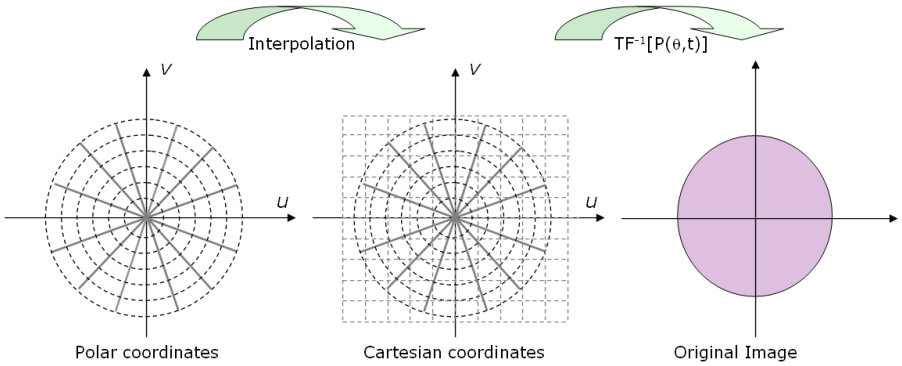

Figure 1-19 Direct reconstructing methods. The left image corresponds with the 2D Fourier transform of the object in polar coordinates, central graphic is the same transform in Cartesian coordinates after interpolation and the image on the left represents the object, after carrying out the inverse 2D Fourier transform. Source: (Abella 2010).

1.2.2.3. Filtered backprojection

The traditional approach to tomographic image reconstruction is based on the filtered backprojection (FBP) method, which is also based on the Central Slice Theorem. It is applied to systems with parallel ray geometry and consists on two clearly distinguished steps: backprojection and filtering.

For an intuitive comprehension of the principal step of FBP method, namely, backprojection, we will use the simple example of Figure 1-20. The image backprojected for the angle $\theta = 0^{\circ}$ is calculated by repeating the attenuation values accumulated for each of the horizontal rays. In the same way, we obtain the backprojected image for angle $\theta = 90^{\circ}$. The final backprojection image will be the sum of the backprojected images for every angle.

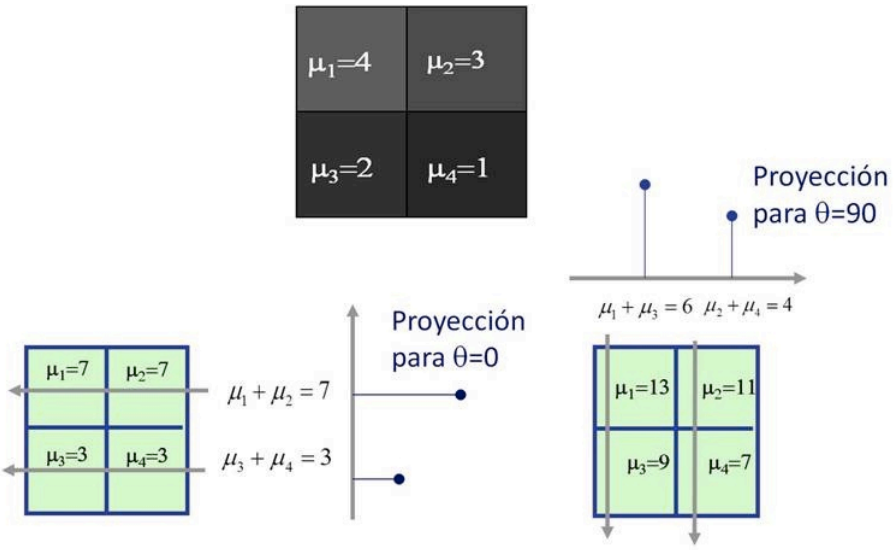

Figure 1-20 Simple example to explain the concept of backprojection. The upper image is the original image, the image on the left is obtained when backprojecting for θ=0º and the image on the right is the sum of the backprojected images for angles θ=0º andθ=90º. The resulting image is not exactly the same as the original one but we can see that it maintains the pixel values distribution.

As mentioned before, for a real case (with more pixels), a bigger amount of projections is needed. Figure 1-21 shows some examples of backprojected images obtained from a different number of projections.

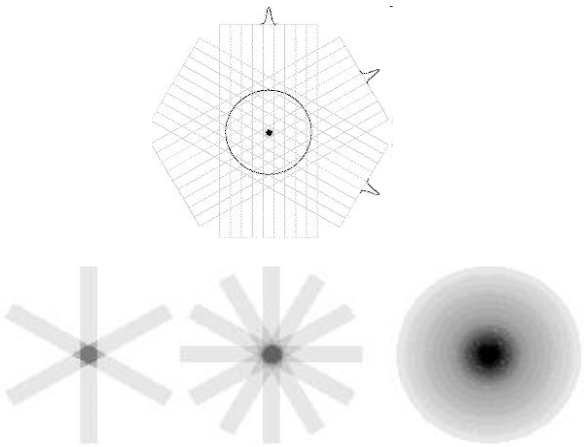

Figure 1-21 Original image, a single dot, projected for different angles (top) and resulting images after backprojection for 3, 6 and 360 angles (bottom); in the last case smoother edges of the spot can be seen.

The image resulting from the backprojection step shows a blurred version of the original image (high low frequency content), being necessary to carry out an additional filtering step to completely recover the image. The formal definition of the method uses the equations below where the filter and the Fourier transform appear:

$$f(x,y) = \int_0^{\pi} Q_\theta(x \cdot \cos\theta + y \cdot sen\theta) \cdot d\theta$$

where

$$Q_\theta(t) = \int_{-\infty}^{\infty} S_\theta(w) \cdot |w| \cdot e^{j \cdot 2 \cdot \pi \cdot w \cdot t} dw$$

This process can be seen on the example shown in Figure 1-22. Figure 1-22a, obtained after backprojecting, is highly blurred due to the highest values concentrated in low frequencies, as can be observed on its 2D Fourier transform (Figure 1-22a'). To enhance the edges and improve the image quality, a 2D cone shaped filter is used (Figure 1-22b), which applies higher weight to high frequency components than to low frequency ones. The result is a better defined image (Figure 1-22c) than the one obtained directly from backprojecting.

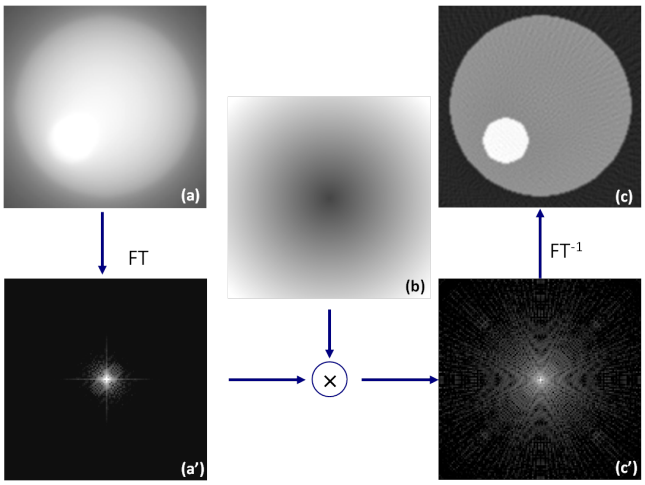

Figure 1-22 Example of the effect of the filtering step in FBP reconstruction.

1.2.2.4. FDK reconstruction

FDK is a reconstruction algorithm for cone beam with circular trajectory proposed by Feldkamp, David and Kreis in 1984 (Feldkamp et al 1984). This method proposes a 3D approximation of the FBP (Turbell 2001), also based in central slice theorem.

For the developing of this method, the problem is faced as it was *FBP* but introducing a third coordinate (axial) in a way that every ray from transformation coordinate system can be considered. Besides, to achieve a more efficient implementation, the real detector coordinates system is matched with the object coordinate system (virtual detector in Figure 1-23).

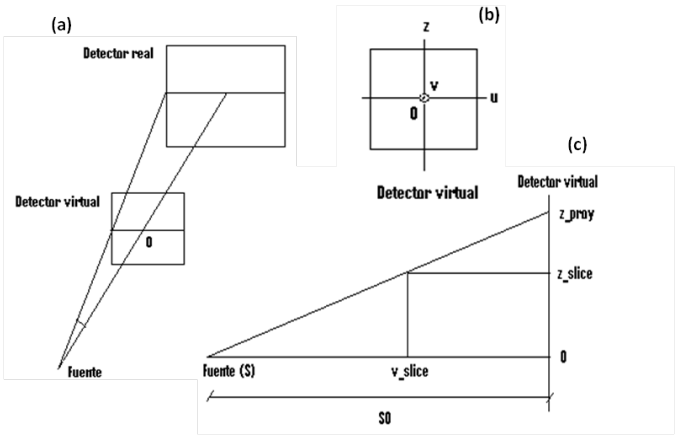

Figure 1-23 (a) perspective view, (b) front view and (c) lateral view of *cone beam* geometry. For reconstruction, real detector coordinate system will be matched with virtual detector coordinate system.

In cone beam with circular path, projections for every angle are obtained. However, these are resultant from different plane combinations. FDK softens the sufficiency condition supposing that the whole volume can be reconstructed slice by slice with the data even they don't complete the Radon space. Actually, just in the central slice there is correct data to apply FBP, so this is the only slice that can be reconstructed without any error. The error will be bigger as the distance to the slice is increased, what is known as cone beam artifact.

The formal definition of FDK method is shown below,

$$f(u,v,z)=\frac{1}{2}\int_0^{2\pi}\frac{v_{FO}}{(v_{FO}-v)^2}\int_{-\infty}^{\infty}R_\beta(s,z)\cdot h\cdot\left(\frac{v_{FO}}{v_{FO}-v}-s\right)\frac{v_{FO}}{\sqrt{v_{FO}^2+z^2+u^2}}\,ds\,d\beta$$

in here, z component appears in the equation.

1.2.2.5. Iterative reconstruction methods

These methods, based in works of Kacmarz in 1937, propose a different way of facing the reconstruction problem: consider the volume to reconstruct a matrix of unknowns and establishing the equations as a function of measured data, resulting the following equation system:

$$\begin{aligned}
&w_{11}f_1+w_{12}f_2+w_{13}f_3+\ldots+w_{1n}f_n=p_1\\
&w_{21}f_1+w_{22}f_2+w_{23}f_3+\ldots+w_{21n}f_n=p_2\\
&\ldots\\
&w_{31}f_1+w_{32}f_2+w_{33}f_3+\ldots+w3_{1n}f_n=p_m
\end{aligned}$$

where f_j is the grey value of the j voxel of the reconstructing volume, p_i the measured value in the detector for the i ray. w_{ij} are the weights defining the influence of the j voxel and i ray. Using a matrix form of the problem it would be:

$$W\cdot f=p$$

W matrix is very large sized (around 100000 TB), so the direct inversion is currently dismissed. The approaching used in iterative techniques, system is resolved by successive approximations

to finally reach a reasonable estimation of the distribution that originated the observed data. This idea is graphically represented in Figure 1-24. The method starts with a simple estimation of the image (formed by ones in the field of view and zeros in the rest in the figure example) that represents an estimation of the real image. Simulated projections of this image are compared for each iteration with the real projections and the error will be corrected in the estimation. The same procedure is repeated until the image that represents the data in a most accurate way is obtained.

Although these methods are computationally expensive, the results are better than analytical method ones in some cases, as for example when the number of obtained projections is limited or these are noisy. These methods allow including a more complete model for the real acquisition process (not just geometry as in the analytical methods), apart from the noise characterization in the statistical methods (type of iterative).

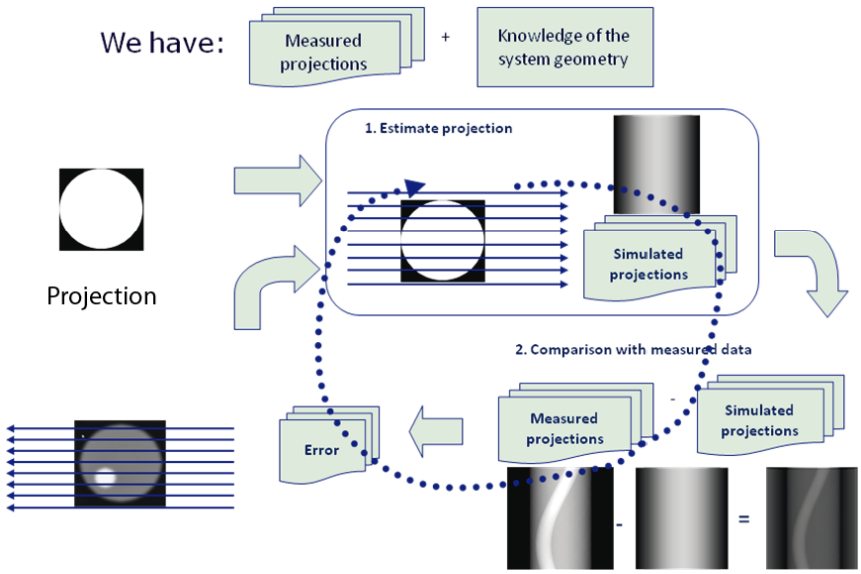

Figure 1-24 Iterative reconstruction methods functioning diagram. Source: (Abella 2010).

1.3. Fluoroscopy

Fluoroscopy is an imaging modality that provides real-time X-ray images. This technique is especially useful for guiding a variety of diagnostic and interventional procedures. A fluoroscope consists on an X-ray source and a detector. Modern fluoroscopes use an image intensifier or a CCD video camera as a detector, which allows the image to be recorded and visualized in a monitor. The ability of fluoroscopy to display motion is provided by a continuous series of images produced at a maximum rate of 25-30 complete images per second (Xue and Wilson 1998), similar to a normal television rate.

While the X-ray exposure needed to produce one fluoroscopic image is low (compared to radiography), high exposures to patients can result from the large series of images that are encountered in fluoroscopic procedures. Therefore, the total fluoroscopic time is one of the major factors that determine the exposure to the patient from fluoroscopy. Personnel working with fluoroscopy equipment must wear proper protection as being exposed to radiation for long periods of time. As seen in Figure 1-25, personnel handling fluoroscopy systems wore minimum protection and worked very close to the device. Nowadays controlling is done remote control and protection is safer.

Figure 1-25 Primitive fluoroscopy procedure in which medical personnel use minimum protection (left) and a photograph of us while working with the C-arm with remote control devices and better protections such as thyroid protection collar (right).

The sensitivity of a fluoroscopic system makes reference to the amount of exposure required to produce images. This will depend on the characteristics of the detector used. The aim is to obtain good quality images that give the specific information required with the less patient exposure possible.

An X-ray image intensifier (XRII) (Figure 1-26) is a large image tube that converts a low intensity X-ray image into a visible image. X-rays incident on an image intensifier are transmitted through an aluminum metal input window with high X-ray transmittance and less scattering. They are then absorbed by an input phosphor screen (cesium iodide crystal) and converted into a light image. On the inner surface of the input phosphor screen, a photocathode is formed, where the light image is converted into a photoelectron image. The photoelectron image is then accelerated and focused by an electric lens (electric field) consisting of an input window, focused electrodes and an anode to collide with an output phosphor screen. The output phosphor screen then, again, converts this photoelectron into a visible light image. Since the photoelectron image is condensed by the electric lens to increase the density of electrons and simultaneously accelerated by a high electric field to collide with the output phosphor screen, the output image is approximately ten thousand times brighter than it would be obtained when the phosphor screen is placed at the input surface position of the X-ray image intensifier. These parts are all mounted in a high vacuum environment within glass or more recently, metal/ceramic.

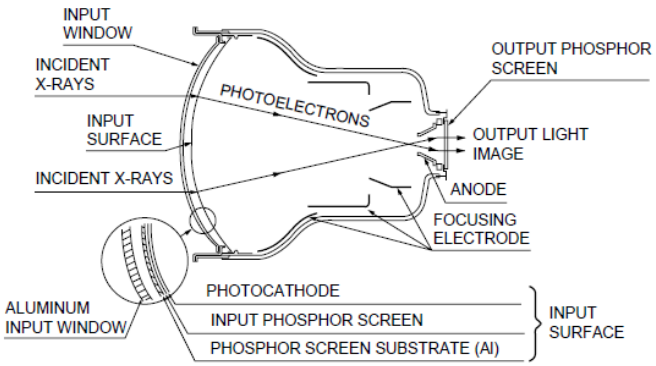

Figure 1-26 Components of an image intensifier tube.

Once the output image is obtained, viewing of the data was via mirrors and optical systems until the adaptation of television systems in the 1960s. The output can now be captured on a camera using pulsed outputs from an x-ray tube similar to a normal radiographic exposure.

A more modern option is the flat-panel detector. As already seen above, flat panel detectors (FPD) use the indirect digital X-ray imaging method, where, in the first place, X-ray photons are converted into visible light by striking a layer of scintillating material. Later these photons strike an array of photodiodes, which converts them into electrons that can activate the pixels in a layer of amorphous silicon. The activated pixels generate electronic data that a computer can convert into a high-quality image of the target, which is then displayed on a computer monitor.

The flat panel detectors are based on amorphous silicon TFT/photodiode arrays coupled to X-ray scintillators. The most common scintillators used in flat panel imaging are the same ones used in standard screen/film radiography and fluoroscopy, gadolinium oxysulfide and cesium-iodide.

1.3.1.Fluoroscopy systems

C-Arm

The mobile fluoroscopic system is known as C-arm (Figure 1-27). It consists of two units, the X-ray generator and the detector (image intensifier or flat panel) mounted in an arc-shaped wheeled structure and the workstation unit used to visualize, store, and manipulate the images. The C-arm allows a great variety of movements, and its characteristic structure makes it possible its use in intraoperative cases, as the arc can be situated around the patient while lying in bed. It is used in different surgical procedures such as cardiology, orthopedics, and urology.

Figure 1-27 C-arm equipment with its storage unit and monitoring cart.

The C-arm should be compact and lightweight to allow easy positioning with adequate space to work around and a wide range of motion while yet remaining inflexible enough so as to minimize misalignments due to flexion caused by the weight of the X-ray tube or the image system assemblies.

Remote controlled X-ray machine

A remarkable area in the radiology equipment market is formed by the systems that can be operated with mechanic or electric remote controllers. These are called remote controlled X-ray machines (Figure 1-28). The aim in this type of equipment is to carry out the greatest number of different explorations with the operator being protected from the radiation located

at a certain distance behind a protective wall. Remote controlled machines are capable of making an examination of the entire body without the need of moving the patient.

Figure 1-28 Remote controlled X-ray machine and its control center.

Remote controlled systems offer a wide spectrum of applications. Fluoroscopic tracing of digestive and intestinal endoscopy studies are frequent, as well as puncture of obstructed liver (nephrostomy). Fluoroscopy systems with image intensifiers are used in these machines in order to fulfill all the requirements needed.

Vascular operating room

The vascular operating rooms (Figure 1-29) are a type of surgery rooms outfitted with specific equipment that allow carrying out interventional radiology. Interventional radiology involves a procedure on the patient using fluoroscopy systems for guiding and monitoring. The idea behind interventional radiology is to diagnose and treat patients using the least invasive techniques currently available in order to minimize risk to the patient and improve health outcomes.

Figure 1-29 Vascular operating room.

2. MOTIVATION, CONTEXTUAL FRAMEWORK AND OBJECTIVES

2.1. Motivation

Radiotherapy (RT) involves the use of ionizing radiation for the treatment of malignant tumors, which is performed in the Radiation Oncology Service of a Hospital. Its main characteristic is the technical complexity of the procedures, the high cost of the equipment and the specific legal regulations that cover not only the products quality control but also the radioprotection for patients and medical staff.

The idea of the radiotherapy treatment is to damage the DNA within the cancer cells. DNA is the genetic code that controls the body's cells behavior. Cancer cells stop growing or die when their DNA is damaged. When the cells die the body breaks them down and gets rid of the waste substances. Healthy, non-cancerous cells in the radiated area may also be damaged resulting in side effects, most of which are temporary because normal tissues are able to repair themselves.

External radiotherapy is the most common form of radiotherapy. It consists on focusing high-energy radiation at the tumor area using a machine called linear accelerator (see Figure 2-1 for illustration). In contrast to internal radiotherapy, in which the radiation source is inside the body, external beam radiotherapy directs the radiation at the tumor from outside the body. X-rays and electron beams are the most common form of radiation in external radiotherapy. Heavier particle beams, particularly proton sources are also used experimental programs

Depending on the tumor different type of radiation is used. In photon therapies, kilovoltage X-rays are used for treating skin cancer and superficial structures and megavoltage X-rays are used to treat deep-stated tumors (e.g. bladder, bowel, prostate, lung or brain). Electron beam therapy is useful for treating superficial lesions because the maximum of dose deposition occurs near the surface and it decreases rapidly with depth. Electron beams usually have nominal energies in the range 4-20 MeV. Depending on the energy the treatment range is approximately 1-5 cm in water equivalent tissue.

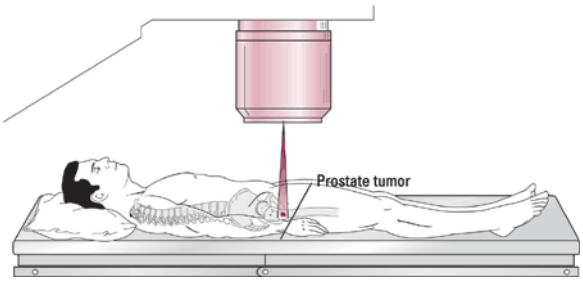

Figure 2-1 Illustration of the linear accelerator and patient during an external radiotherapy in the treatment of prostate tumor.

A radiotherapy treatment must be carefully planed, based on a previous study of the dose needed to treat the tumor the areas of interest and possible areas of risk. The specialist must decide the exact area to be treated allowing for possible movement of the tumor during treatment due to breathing or normal movement of body organs. The planning makes sure that the tumor gets the prescribed dose of radiation while normal body tissues get as little as

possible. The importance of protecting the critical organs and structures from radiation lies on their particular organic response to radiation. This includes the response of the radiated organs separately as well as the entire organism exposed to radiation. The response of a system or organ is defined as the morphological and/or functional changes produced by a determined dose in a certain time interval. Dosimeter calculation is done from CT images of the patient alone or merged with other modalities to obtain complementary information (such as NMR or PET/CT images). These images are introduced in specific software that allows for the calculation of the dose distribution by evaluating the interaction of the radiation beams with the interacting tissues.

The goal of Intraoperative Radiation Therapy (IORT), based on the external radiotherapy techniques, is the precise irradiation with a high dose of post-resected tumor beds or partially resected tumors right after the surgery (Figure 2-2). It can also be performed both with electron and X-ray beams.

IORT has several advantages over external RT: the tumor bed where the highest dose should be applied is frequently missed in external radiotherapy due to the complex localization of the wound cavity. Since IORT is performed with the patient opened, it helps directing the dose to the area of interest while reducing the radiation of surrounding tissues, which can be displaced or shielded during the IORT. The most common intervention areas in IORT are abdomen, breast, rectum and extremities. Critical structures such as lungs, small intestine, cardiovascular tissue and bone tissue must be protected during the radiation due to its proximity to these irradiated zones.

Figure 2-2 Intraoperative Radiotherapy procedure where surgical staff placing the Lucite tube into patient's body.

Additionally, the usual delay between the surgical removal of the tumor and external radiotherapy may allow a repopulation of the tumor cells. This can be avoided by delivering the radiation directly to the targeted tissues leading to immediate sterilization of residual tumor cells. Also, IORT was found to inhibit the stimulating effect on tumor cells of the wound fluid (Massarut et al. 2008).

One of the current main limitations in IORT lies in the difficulties that the therapy planning process entails. It is difficult to carry out a feasible dosimetry calculation from pre-operative images due to the retraction of the patient's structures and the removal of affected tissues that modify the patient's geometry. This fact brings up two problems for the planning:

- Before surgery: it is complex to estimate the dose that should be applied.
- After surgery: since the image of the exact anatomy not available, the dosimetry cannot be calculated.

In addition, as in IORT an applicator has to reach the tissues to be irradiated (Figure 2-3), the surgical area and all the monitory systems has to be adapted in order to have an open access to the tumor bed. Also, the whole area and any instrumentation, including the applicator, has to be sterilized, and the procedure is even more complicated when the accelerator is not in the surgical room and the patient has to be moved.

Figure 2-3 Intraoperative Radiotherapy procedure. The medical staff is placing the applicator in the radiation source.

Currently, it is very difficult to plan the IORT process beforehand; that is why the surgeons must choose during surgery the cone dimension, its positioning, the bevel angle and the electron beam's energy according to their experience and the information gathered during surgery. This means that the previous dosimeter estimation of the radiation to be applied is not good enough to properly assess, with certain precision, the results obtained (complete scope of the tumor bed, dose on healthy tissues and critical organs, etc.). Therefore the possible beneficial and deleterious effects of irradiation cannot be precisely assessed.

2.2. Contextual framework of the project

The development of volumetric imaging systems for the purpose of guiding radiation therapy is a topic of a major interest in radiation therapy (Jaffray et al. 2002), (Hesse et al. 1998). Integrating this technology with the medical linear accelerator is believed to have excellent potential as a platform for high-precision, image-guided RT.

In this context, GMV in collaboration with the imaging group at Gregorio Marañón Hospital developed the first IORT-planning tool called *radiance*. This tool allows the estimation of the dose distribution delivered to the target tissues and organs at risk based on a pre-operative CT. The incision made by the surgeon to resect the tumor is resembled with a specific facility called surgical frame, which also identifies the entry point of the applicator. A 3D graphic engine provides high quality Multi-Planar Reconstruction and volumetric visualization of the patient (Figure 2-4).

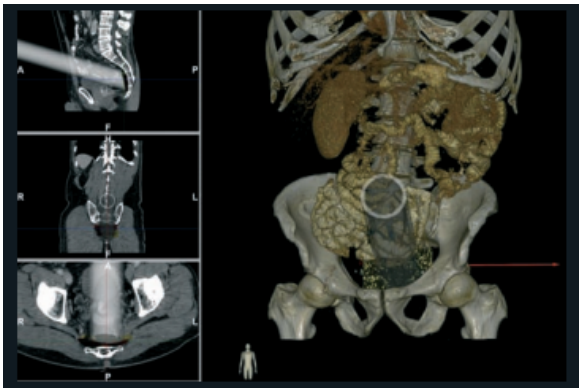

Figure 2-4 Example of an IORT planning simulation created by *radiance*, using a previous CT image.

radiance allows the segmentation of tissues of interest (tumor bed and organs at risk). Then, the applicator is virtually placed at the best location to optimize tumor bed coverage, and the tool calculates the dose that will be delivered to those tissues for a given diameter, angle of the applicator and energy applied. The radiation oncologist can find an optimized solution that maximizes radiation dose to the tumor bed and minimize it in the organs at risk before or during the intervention (Figure 2-5).

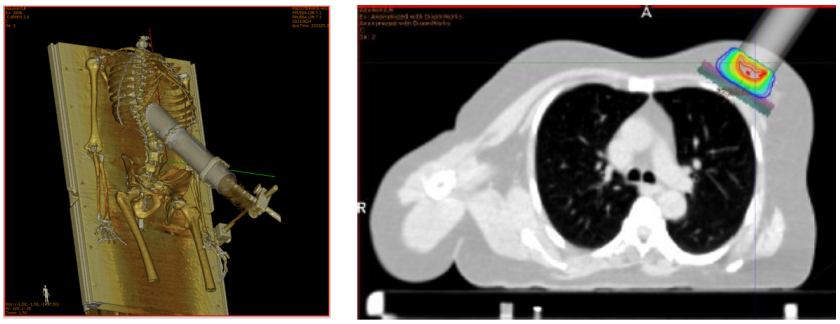

Figure 2-5 Radiance simulates dose range received by the application surrounding tissues depending on their properties, dose energy and application angle.

Still, the complete evaluation would need an imaging technique during surgery to know the real scenario during the treatment.

One proposal from the imaging group at Gregorio Marañón Hospital is to use a C-arm scanner, originally designed to obtain planar images, as a tomograph to obtain 3D images of the patient during IORT due to its versatility and wide variety of movements. The C-arm working as a tomograph will be analog to a CT scanner with cone-beam geometry.

The use of a C-arm for tomography presents several difficulties. It may have mechanical strains and looseness in the detector (image intensifier) and the movements of source and detector may differ from a circular path. Moreover, it is necessary to consider the repeatability of the acquisitions for same positions at different moments.

In order to obtain good quality images, it is necessary to evaluate the effects of these non-idealities and to perform an exhaustive calibration of the system, not needed when it is used for planar imaging Additionally, it will require accurate geometric calibration to overcome these effects (Cho et al. 2005).

2.3. C-Arm SIREMOBIL Compact L. Siemens.

The system SIREMOBIL Compact L (*Siemens*), available in the UMCE, is a mobile X-ray equipment for its use in surgery, orthopedic surgery, minimum invasive surgery and cardiology (Figure 2-6). This C-arm can perform different functions as scopy, pushed scopy and digital radiography, which are necessary for a wide variety of clinical procedures such as intraoperative visualization of bile ducts, metallic element implant, bone visualization, scopy techniques for pain treatments and insertion of catheters.

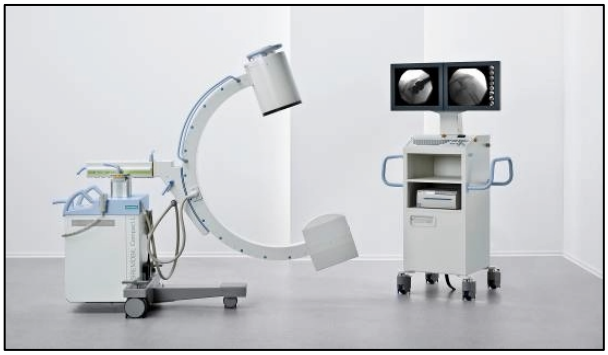

Figure 2-6 SIREMOBIL Compact L (Siemens) C-arm.

Images can be visualized in a TFT monitor. The visualization of the object in the monitor of the C-arm depends on the position of the unity regarding to the patient and is explained in Figure 2-7:

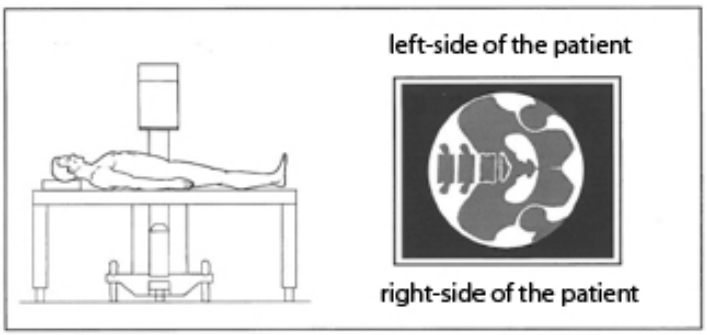

Figure 2-7 Illustration of the obtained projection according to the position of the C-arm.

These images can be exported to a PC through a USB port using an external video-capture device. The model of the used is NPG USB RealStudio II (Figure 2-8), which can copy static images and video data into the connected computer.

Figure 2-8 NPG USB RealStudio II capture card.

The SIREMOBIL consists of an X-ray source based on a monofocal tube with a 1,4 kW generator and a 23 cm diameter circular image intensifier with an anti diffusion grid attached to a C-Arm gantry.

As the C-arm system has the objective of adjusting its position to the requirements of the procedure and patient, it has handles that facilitates wide variety of movements its movement (Figure 2-9). The whole C-arm can be horizontally freely moved when brakes are released for displacement from one place to another.

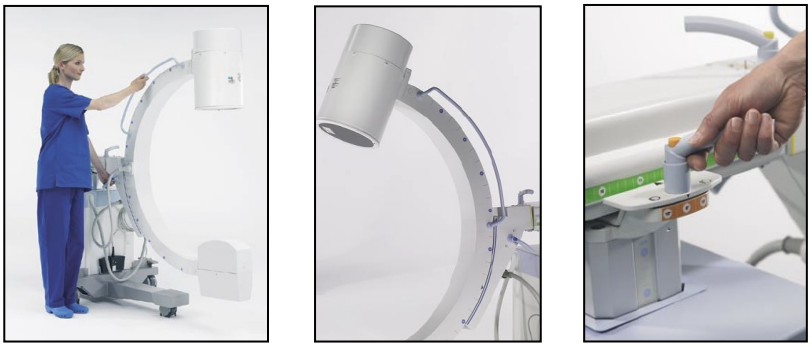

Figure 2-9 Detailed images of the movement possibilities of the C-arm.

With the purpose of approaching to the bed regarding to its height and depth, C-arm allows 45 cm elevation from its lowest point and 20 cm horizontal displacement (Figure 2-10).

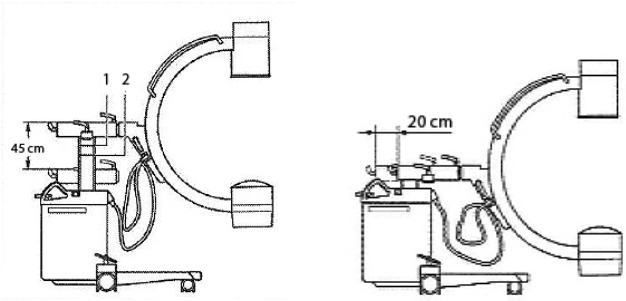

Figure 2-10 Illustration of elevation (left) and horizontal (right) displacements of the C-arm.

The C-arm can rotate around two different axes in order to place with certain perspectives regarding to the patient. This allows obtaining images of the region of interest from different angular positions. We will refer to the two rotations that the system is able to perform are the angulation and the orbital movement:

- Angulation is a rotation around the horizontal supporting arm and spans more than a 360º (Figure 2-11).

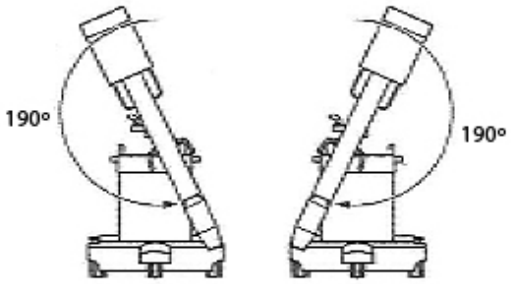

Figure 2-11 Angulation movement.

- Orbital movement consists on a rotation on the C-arm plane and spans a range from +90º to -40º starting from the neutral position (Figure 2-12)

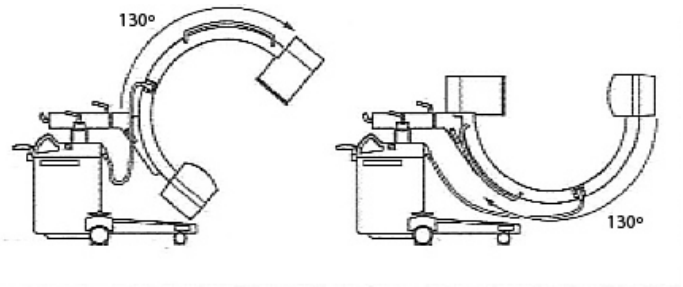

Figure 2-12 Orbital movement.

Considering the objective of using this system as a tomograph, we can rotate the C-arm around the bed using one of the two turning options permitted. The arc shape of the C-arm makes the orbital movement less susceptible of suffering deformations being more stable than the angulation movement. Nevertheless, there is a rotation limit of 130º for this movement, which does not allow for obtaining a complete set of projections around 360º, while angulation movement allows full rotation.

Finally, the gantry is mounted on a wheeled module with steering handles that allows for the easy movement of the whole system.

There is technical information of the C-arm model on appendix B at the end of the document.

2.4. Review of calibration techniques

As mentioned above, we propose to use a C-Arm as a tomograph to obtain 3D images of the patient during IORT. In that sense, the C-Arm will work analogously to a CT scanner with cone-beam geometry. The use of a C-arm for tomography presents several difficulties. It may have mechanical strains and looseness in the detector (image intensifier) and the movements of source and detector may differ from a circular path due to gravity-induced flex in the support arms (Cho et al. 2005). Besides, distortion caused by the image intensifier deforms the projections images, being a problem that must also be corrected when using the C-arm for planar images (Vendantham et al. 2000). Also, the repeatability of the acquisitions for same positions at different moments must be considered.

In order to obtain good quality reconstructed images, it is necessary to evaluate the effects of these non-idealities and to perform an exhaustive calibration of the system, not needed when it is used for planar imaging. A complete geometric calibration involves the estimation of a set of parameters that determine the geometry of the system.

In the literature we find different options to measure these non-idealities in X-ray systems similar to the one under study. In (Fahrig and Holdsworth 2000; Jaffray et al. 2002), the authors explore the misalignment problem of radiography systems integrated with a medical linear accelerator. The calibration is based on projection images of a metal sphere placed in the isocenter of the FOV; assuming that the source travels in a circular trajectory, non-idealities in the motion trajectory can be modeled by identifying the position of the center of the sphere on the projections. Nevertheless, this simple technique does not obtain a complete description of geometry of the system, omitting many of the non-idealities present in real equipment like rotations and inclinations on the detector plane.

Many methods for the estimation of geometrical parameters of cone-beam scanners have been proposed since 1990 (Noo et al. 2000; von Smekal et al. 2004; Cho et al. 2005; Sun et al. 2006), These techniques are based on the direct solution of geometric equations. For example, the

method described in (Noo et al. 2000) is robust, easy to implement and uses a simple calibration object based in two metallic spheres. The disadvantage of this method is that it assumes that the system is isocentrical, which is generally not the case with C-arm systems.

Several works describe the calibration of the imaging system based on the projection matrix concept (Rougee et al. 1993; Navab et al. 2003). The general idea was developed in computer vision and it represents a mapping from 3D object coordinate system to 2D projection image plane. The projection matrix, based on the *pinhole camera model,* can be determined experimentally through the imaging of a phantom made of markers with known geometry.

The advantages of this procedure include: (1) it is capable of being applied to systems of different scan trajectories, source-detector alignments, and detector orientations; (2) projection matrices can be utilized in image reconstructions with the extraction of explicit geometrical parameters; and (3) the method imposes minimal limits on the design of calibration phantom. Nevertheless, the calculation of the parameter from the projection matrix is difficult and unstable (Rougee et al. 1993; Fahrig and Holdsworth 2000).

Therefore, a method that estimates directly these parameters has advantages over the projection matrix method as the complete set of parameters can be used in numerous applications and in different devices. Cho et al. presented a method that generates a complete description of the geometric parameters by analyzing a single projection. The method allows the estimation of the geometrical parameters (e.g., rotation of c-arm, detector inclination, detector shift) with high accuracy from a single X-ray image of a calibration phantom. In this work, we are going to base the calibration of our system on this last method.

2.5. Objective

The C-arm equipment is not specifically designed to work as a tomograph, so it is unstable and presents significant geometrical non-idealities. Therefore, a calibration must be done in order to get a good quality reconstruction of the volume.

The general objective of the thesis is to evaluate the non-idealities that hinder the use of a C-arm as a tomograph and to develop a calibration method.

This general objective is divided in the following specific objectives:

1. Analysis of the system under study. The first phase consists on the analysis of the system to comprehend the basic principles of working. The data acquisition processes, principal sources of error that limit the quality of the obtained images. Since the goal is to use the system as a tomograph, this phase also includes acquiring an understanding of image reconstruction principles and algorithms.

2. Study and characterization of stability and repeatability of the acquisitions of the C-arm of the laboratory. This phase consists of the study and characterization of the equipment non-idealities that may affect the acquired images as well as geometrical misalignment effects on reconstructed images. Development of a simulation tool to reproduce artifacts produced by non-idealities.

3. Implementation of a calibration algorithm that obtains geometric parameters from a set of projections and design of the phantom used in the calibration algorithm.

To evaluate the tasks during the project we will use the infrastructure available in the Medical Unit and Experimental Surgery (UMCE) in Gregorio Marañón Hospital (HGGM).

2.6. Outline of the manuscript

The manuscript consists on the following chapters:

- **Chapter 1: Introduction**. We describe the physical basis of the X-rays, their generation and detection, and different types of detectors. Then, X-ray tomography functioning is defined together with the concept of projection and the reconstruction process. Finally, fluoroscopy concept and fluoroscopy equipment are presented.

- **Chapter 2: Motivation, contextual framework and objectives.** In this chapter we introduce the intraoperative radiation techniques and the context of the thesis. That includes a description of C-arm equipment available in the laboratory are shown and a review of the calibration techniques found in the bibliography. Finally, the objectives of the thesis are presented.

- **Chapter 3: Evaluation of the error sources.** In this chapter we present the evaluation of the possible error sources present in our system. These are divided in distortion effect, a study of the repeatability and stability and an evaluation of geometrical misalignments. For this last study a simulation tool is implemented to emulate the functioning of the C-arm. It produces a set of projections of synthetic phantoms based on the parameters that describe the real system introducing the misalignments characterized for the equipment. Using this software tool, the effect of geometrical misalignments on the reconstructed images is described, as well as the tolerance of these effects.

- **Chapter 4: Calibration method.** In this section we make a review of the different calibration methods found in the literature and we describe the calibration method implemented for a C-arm available in Experimental Medicine Unit in Gregorio Marañón Hospital in Madrid based on the work by (Cho et al. 2005). Finally, results obtained with this method are presented.

- **Chapter 5: Discussion and conclusions.**

- **Chapter 6: Future works.**

3. EVALUATION OF ERROR SOURCES

This chapter presents an evaluation of the effects of the non-idealities of the system. These non-idealities include distortion on the images due to physical phenomena in the image intensifier and geometrical misalignments of the tube and detector with mechanical origin. We evaluate the distortion using real acquisitions, studying also the stability and repeatability of the system. For the study of the geometrical misalignments we develop a simulation software that models the behavior of the system when certain misalignments are present.

3.1. Study of the distortion caused by the image intensifier

Every image intensifier shows a certain grade of distortion in the lines and vignetting. This may be caused by the magnetic contamination of the image tube or by the installation of the image intensifier within a large magnetic field, which may affect the trajectory of electrons travelling inside the tube from the input phosphor screen to the output phosphor (see Figure 1-26) (Vendantham et al. 2000).

We can find two different effects of distortion:

- S-type distortion makes imaging of a straight object to appear having an S-shape. It is caused by the influence of the earth's magnetic field on the trajectories of electrons inside the image intensifier tube. In order to avoid it, the image intensifier is shielded with a material called "mu-metal" but, in most cases, a significant amount of s-type distortion reminds. Most troublesome is the fact that the s-type distortion may change spatially as the intensifier is moved around the patient (Figure 3-1).

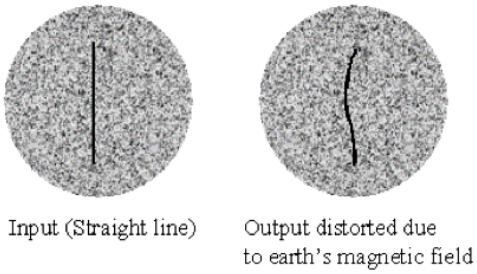

Figure 3-1 Illustration of the S-type distortion. The image of a straight-line object appears distorted at the output of the image-intensifier. Figure from (Vendantham et al. 2000).

- Pincushion and barrel-type distortions are caused by the inherent limitations of the electron focusing optics (Figure 3-2).

Figure 3-2 Illustration examples of the barrel and pincushion-type distortions. Image shows an undistorted squared input (left), barrel-type distortion (center) and pincushion-type distortion (right). Figure from (Vendantham et al. 2000).

To evaluate the distortion in our C-arm, we used a phantom consisting of an old electronic board with radio-opaque cupper straight lines with right angles (Figure 3-3). For the acquisitions, the phantom was attached to the intensifier outer casing.

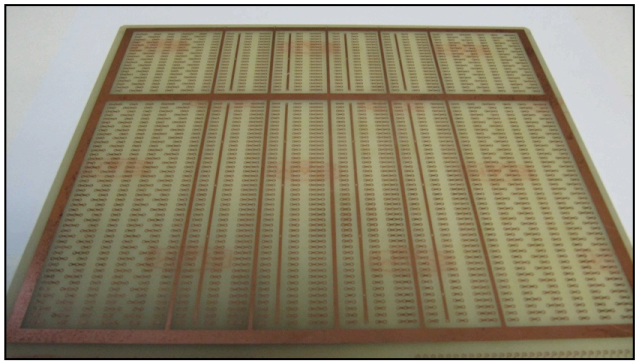

Figure 3-3 Electronic board consisting of cupper layers on a plastic plate used to evaluate distortions in the image intensifier.

To study the straightness of the lines on the projection we did an analysis using IDL 6.4. We took five profiles along the line patterns on the projection images (shown in green in Figure 3-4). The dots showed a straight pattern indicating no significant distortion in the image intensifier according to the effects found in the literature.

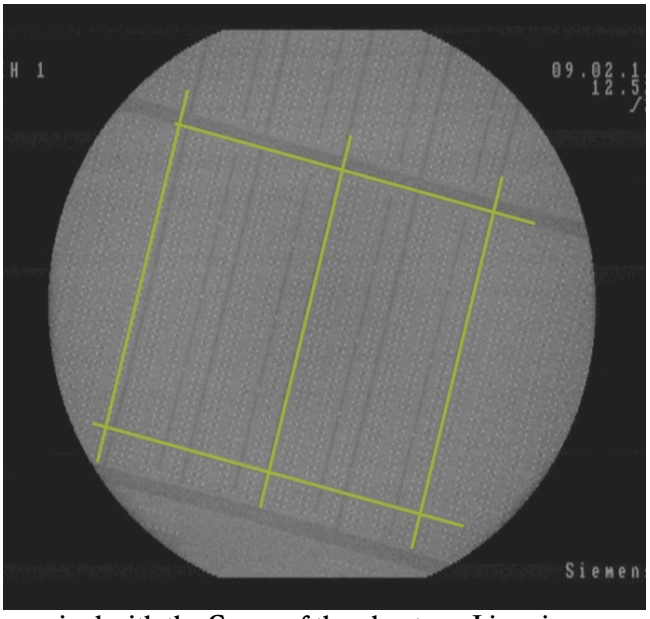

Figure 3-4 Projection acquired with the C-arm of the phantom. Lines in green are straight, matching with the lines of the projection of the phantom.

Nevertheless, it is appreciated that the projection show an oval shape while it should be a circle as it is the shape of the image intensifier detector (Figure 3-5). Green lines show ideal shapes (90º angles and a perfect circle). The angles shown are about 88º and the major diameter of the ellipse is ~8% bigger than the diameter corresponding to a circle (green line).

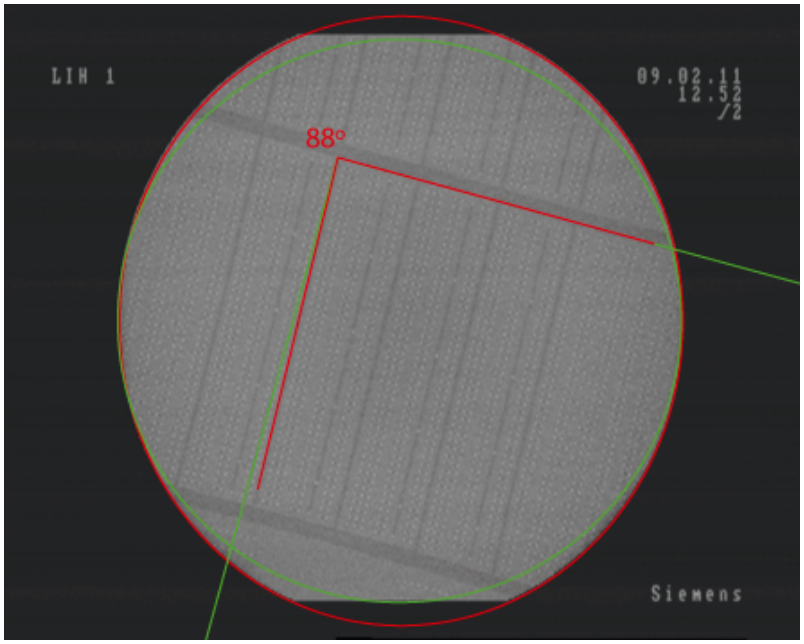

Figure 3-5 Projection acquired with the C-arm of the phantom. Red lines follow the pattern (lines and circle contour). Green lines show the ideal directions and shapes of the phantom.

Since this effect does not correspond with any characteristic effect of distortion, we assumed that the obtained projection needs a scaling in vertical axis to correct it. The solution to this problem is to apply a geometrical transformation to the acquired image consisting on a scaling of 1.08 on the *y* coordinate, given by:

$$\begin{pmatrix} x' \\ y' \\ 1 \end{pmatrix} = \begin{pmatrix} 1 & 0 & 0 \\ 0 & 1.08 & 0 \\ 0 & 0 & 1 \end{pmatrix} \begin{pmatrix} x \\ y \\ 1 \end{pmatrix}$$

3.2. Study of the stability

To study the stability and repeatability of the system we did four sets of acquisitions with the C-arm. The concept of repeatability makes reference to variation in measurements taken by a single instrument on the same item and under the same conditions. With stability of the system, we mean the rigidity of its movements and the resistance to deformations.

Each one of the four sets of acquisitions was done in order to analyze the behavior of the equipment in different aspects:

- Acquisition set #1: Repeatability in single and different positions.
- Acquisition set #2: Stability of the two rotation options.
- Acquisition set #3: Repeatability in a single position after movements.

– **ACQUISITION SET #1: Study of repeatability in single and in different positions.**

This set of acquisitions is done with a phantom consisting on a piece of cardboard with radio-opaque wires stuck in it (Figure 3-6). These projections are taken with the phantom attached to the C-arm case.

Figure 3-6 Photograph of the paper phantom attached to the C-arm intensifier case.

30 projections are taken for each one of the four different positions of the C-arm shown in Figure 3-7, varying orbital and angulation rotations on each one.

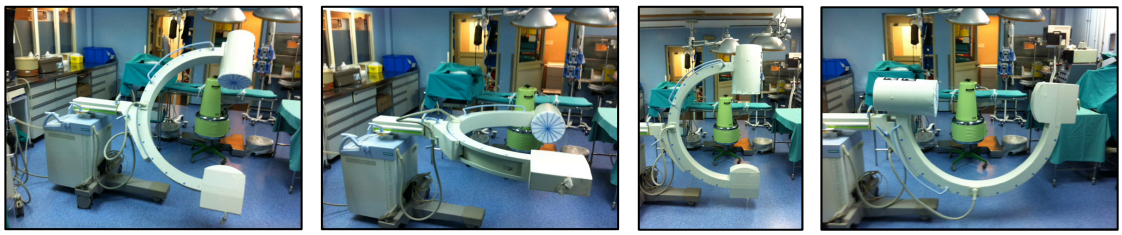

Figure 3-7 Different angular positions of the C-arm in which the projections are done.

First, we study the stability of the system when acquiring images in the same position. Figure 3-8 shows the thirty projections merged together in one image indicating that there is no significant misalignment between positions.

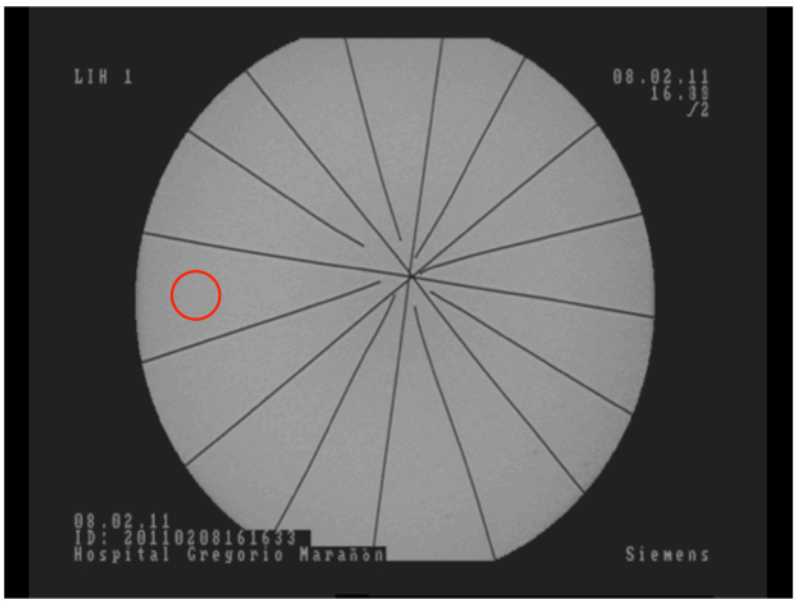

Figure 3-8 Thirty projection images taken continuously for same position of the C-arm put together in one. Clearly defined lines show no difference between acquisitions.

To quantify the stability of the intensity values, we measured the mean intensity value on the homogeneous region of interest (ROI), shown in Figure 3-8. Results show that the variation between different acquisitions is negligible (<1%).

Secondly, we performed the same analysis for images acquired in different positions of the C-arm. The image in Figure 3-9 corresponds to the four projection images merged, showing a mismatch.

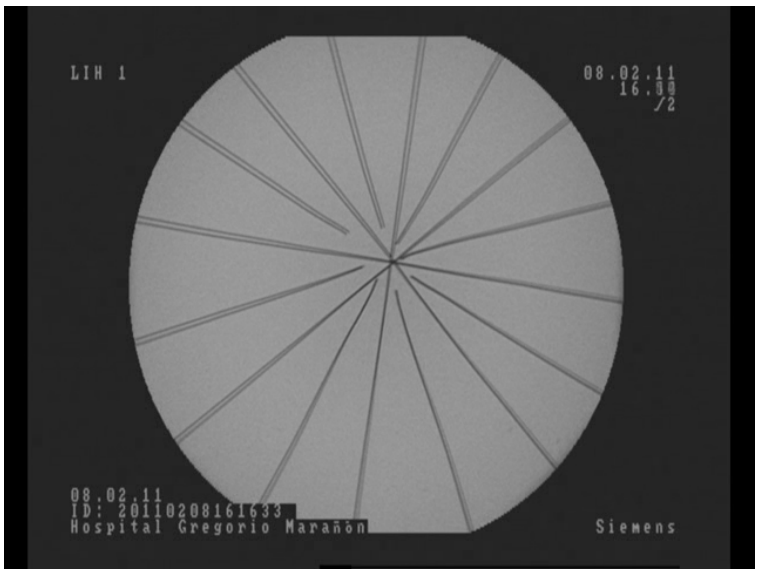

Figure 3-9 Four projection images taken for different positions of the C-arm put together in one. Blurry lines show differences between acquisitions. The red dot indicates the region of interest where mean values of grey in each projection are measured to study the differences.

As same as done before, we measured the mean intensity value for the same ROI on the 30 projections for each one of the four positions. Figure 3-10 shows the mean values measured on 30 projections for each one of the four positions indicated in Figure 3-7.

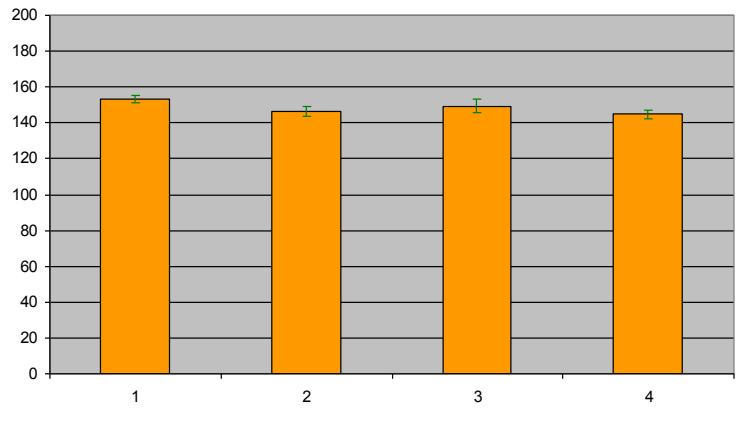

Figure 3-10 Mean values and standard deviation for the four positions shown in Figure 3-7.

The value standard deviation along positions is σ/μ=3,748. According to these results, we can conclude that there is no significant difference between different positions. However, looking at the projections mismatch on Figure 3-9, we can say that the equipment has low repeatability for different angular positions of the C-arm.

- **ACQUISITION SET #2: Study of stability of the two options of rotation**

The aim of this experiment is the identification of the most stable rotation movement of the C-arm. We study the behavior of the C-arm in response to movements along its angulation and orbital rotations (Figure 3-11).

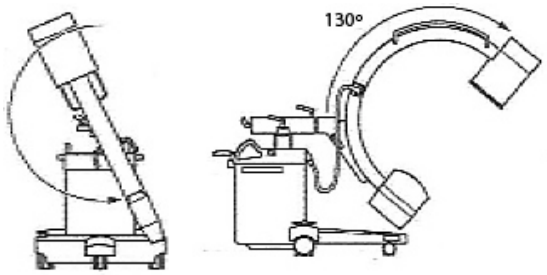

Figure 3-11 Angulation (left) and orbital (right) movements.

We used the phantom shown in Figure 3-12. Designed originally to obtain a camera calibration of X-ray systems, it consists on 24 ball bearings distributed in 4 parallel planes and forming rings of 6 balls at different heights and with decreasing diameters. Using such a phantom, where the metallic patterns are far away from the detector, allows obtaining better information of the effects of the C-arm deformations on the projections.

Figure 3-12 Camera calibration phantom attached to the C-arm image intensifier case.

One projection is obtained after each time we vary the position in one of these two movement options while maintaining the other one constant.

- Orbital position is defined by θ. Figure 3-13 shows the merged images of several projections made for a constant value θ=80º, while **varying angulation value ϕ.**

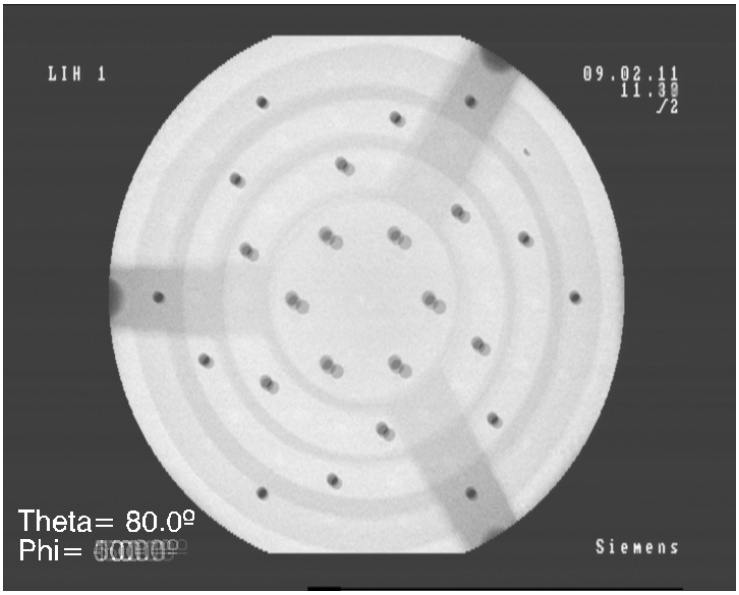

Figure 3-13 Six projection images taken for an orbital angle of 80º while varying angulation values (from -150º to 100º) put together in one. Misalignments are large especially on the inner circles, which are further from the detector plane.

- Figure 3-14 shows the merged images of several projections made for a constant value of angulation ϕ=-50º, while **varying orbital angle θ**.

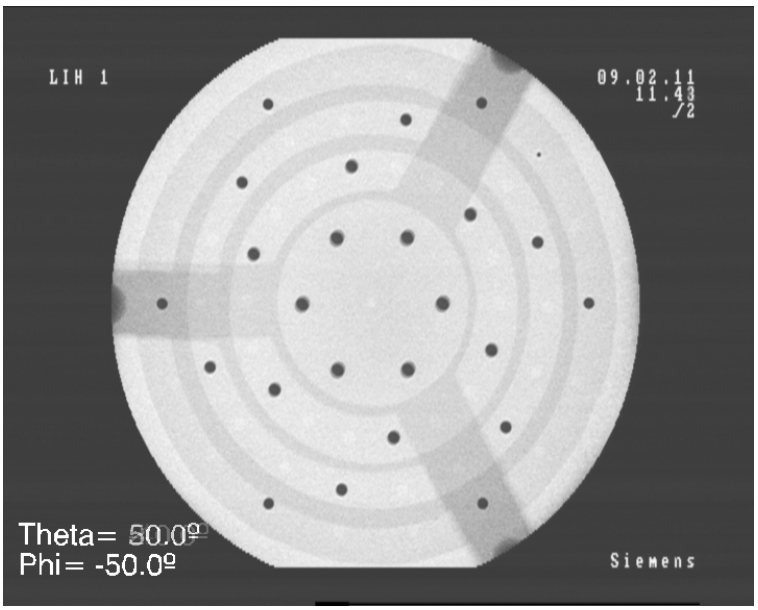

Figure 3-14 Four projection images taken for an angulation value of -50º while varying orbital movement (from -40º to 50º) put together in one. Misalignments are visible on the inner circles, which are further from the detector plane.

From the presented results, we can see that when acquiring images at different angulations (without varying the orbital position) results are less stable. This is most likely due to the fact that the C-arm is more resistant to deformations on the vertical plane (perpendicular to the floor). In fact, C-arm systems normally make use of the orbital movement to get a good positioning regarding to the patient. The problem is that orbital movement has a rotation limitation of 130º, not allowing to obtain projections covering 360 degrees, which are ideally used for image reconstruction. In contrast, the more unstable movement (angulation) allows a complete 360º rotation around the patient.

- **ACQUISITION SET #3: Repeatability study for a single position after applying intermediate movements to the C-arm.**

The purpose of this experiment was to evaluate the repeatability of the system when acquiring images at the same angular position after performing intermediate movements. In the experiment, the C-arm was moved from its original angular position (where a first projection was taken) describing a random path along orbital and angulation movements before going back to the same position to make next projection. This process was repeated to obtain a third projection. The phantom used is the four-ring phantom used in previous set of acquisitions (Figure 3-12).

If the system were ideal exactly the same projection image should be obtained, as same position of the C-arm would lead to an identical response. However, hypothetical looseness in the image intensifier or mechanical deformations of the arc could affect negatively.

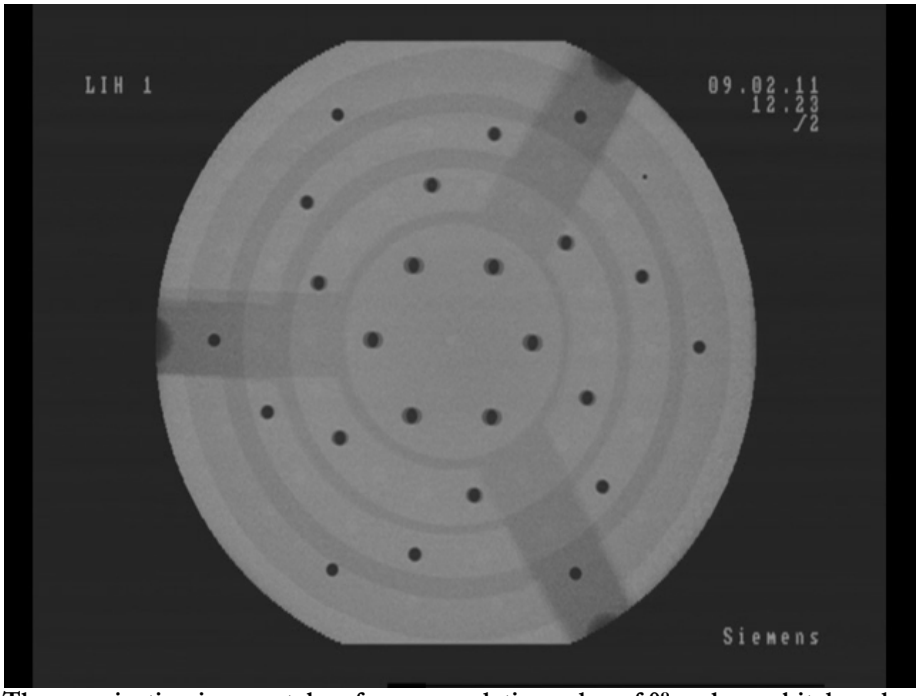

Figure 3-15 Three projection images taken for an angulation value of 0º and an orbital angle of 0º put together in one. Misalignments are large on the inner circles, which are further from the detector plane.

As shown in the Figure 3-15, differences on the projections can be noticed for balls of inner circles. This suggests low repeatability of the system after intermediate movements, although results may be biased due to the fact that it is difficult to assure that the C-arm was again placed in the same exact location as before, as positioning marks are visual and not very precise.

All acquisitions (cardboard phantom and 24-ball phantom) were done with the object attached to the C-arm case. This fact may introduce a new source of error since it is unknown if the case protecting the structure, the image intensifier, and the X-ray source move as a whole with the rest of elements or if there is some looseness and/or deformations. For this reason, experiments involving calibration of the C-arm were performed using a phantom not attached to the C-arm in order to study the complete geometry (Daly et al. 2008).

3.3. Study of geometrical misalignments

Another group of non-idealities in the C-arm are those due to mechanical misplacements (misalignments) from the ideal positions of both source and detector, resulting from the tolerances in the manufacturing process. Additionally, mechanical flex suffered by the C-arm in different positions, caused by the heavy loads at its ends, can make the geometry parameters further differ from the nominal values (Jaffray et al. 2002).

The misalignments that might be present in a C-arm system are, on one hand, those related to the detector including inclinations out of the detector plane (roll and tilt), rotation (skew) and translation in X and Y of the panel detector, shown in Figure 3-16.

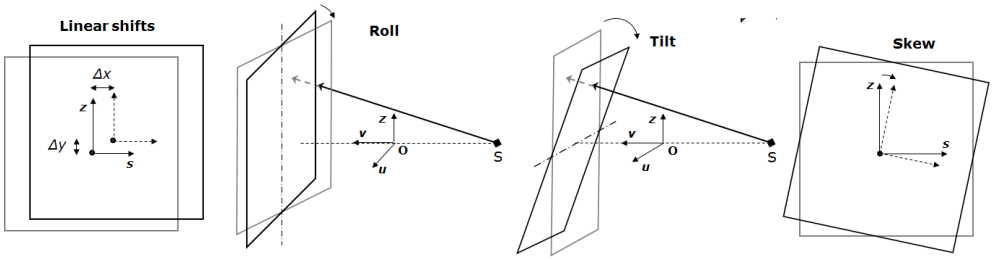

Figure 3-16 Linear shifts, roll and tilt out of the detector plane, and skew (in the detector plane) . [z, s] and [u,v,z] are the coordinate systems in the detector and the FOV respectively and S represents the position of the X-ray source.

On the other hand, the mechanical flex of the C-arm, which may lead to changes in source-detector distance, is considered as another geometrical misalignment Figure 3-17

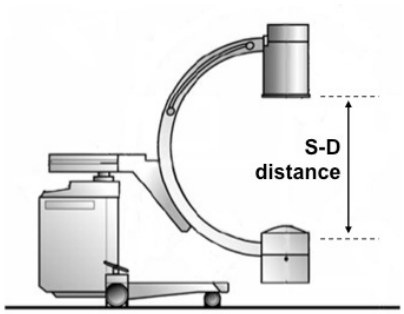

Figure 3-17 Source-detector distance may change due to deformations of the arm

We developed a software simulation tool, to study the effects of the possible misalignments both on the projections and the reconstructed image, including effects of linear shifts, skew, roll and tilt in the image intensifier plane and variations in the source-detector distance. The analysis of results enables the estimation of the acceptable misalignment range (tolerance) for each value.

The simulator emulates the functioning of the C-arm system under study: it produces a set of projections of synthetic phantoms based on the parameters that describe the real system (C-Arm Model SIREMOBIL Compact L of Siemens, shown in Figure 3-18). Data reconstruction is done with Mangoose, a multi-bed reconstruction software based in the FDK analytical method (Abella et al. 2012).

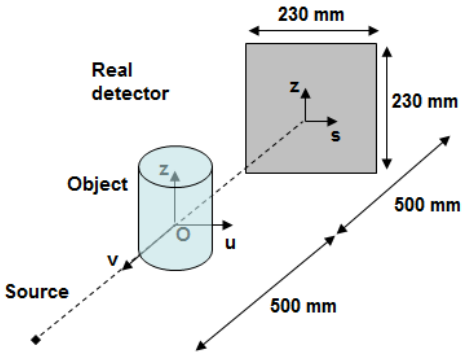

Figure 3-18 Descriptive illustration of the C-Arm Model SIREMOBIL Compact L of Siemens.

The simulation tool, implemented using IDL 6.4 (ITT Visual Information Solutions, Boulder, CO), consists of three independent modules: "phantom creation", "projection" and "offset and skew". A flowchart describing the whole process is shown below on Figure 3-19.

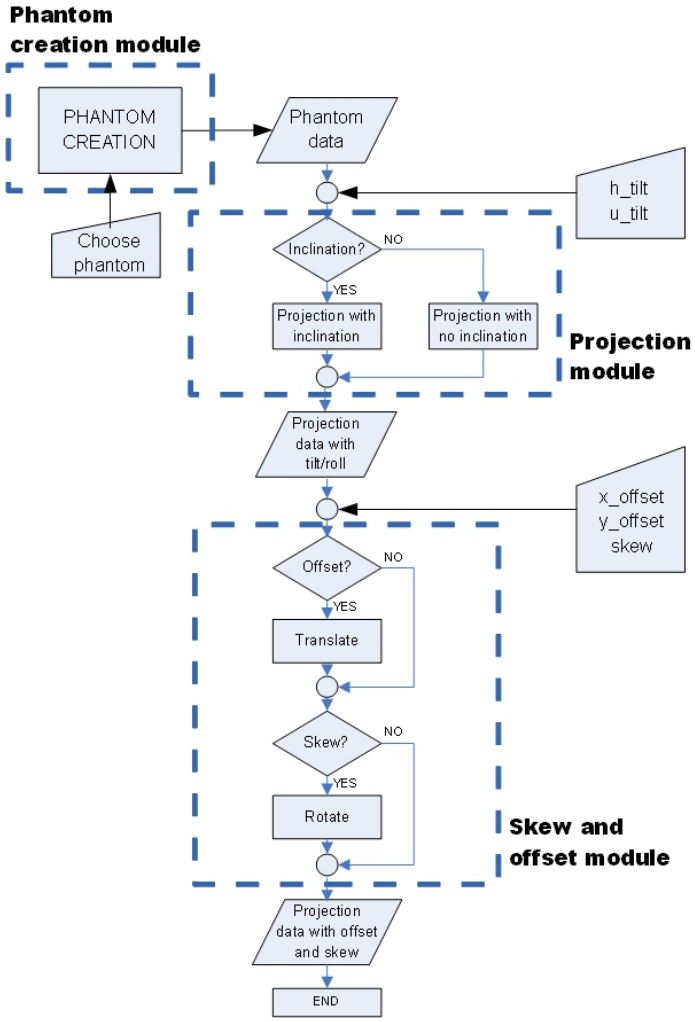

Figure 3-19 Flowchart of the simulation tool.

The inclinations out of the detector plane must be introduced in the projection module and linear shifts and rotations of the detector are simulated once the tilted projection is made.

3.3.1.Phantom creation module

The simulator creates three synthetic phantoms with similar attenuation characteristics to human bones and soft tissue based on cylinders and spheres. For the evaluation of misalignment effects we have used two of the phantoms shown in Figure 3-20, as the third one is used with other purpose later in the project.

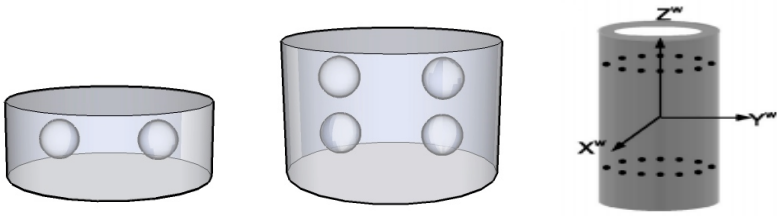

Figure 3-20 Illustration of the three different phantoms created by the simulator. Its sizes are Ø80x40 mm (left) and Ø80x66. mm (center) and Ø70x70 mm (right).

The size of the phantoms is designed to fit in the FOV of our system detector, which is 114.4 mm diameter. The pixel size is 0.8 mm (detector binning of 2), resulting in:

- Phantom 1: a methacrylate cylinder of 50x100 pixels (height and diameter respectively) with two spherical balls inside of 20 pixels diameter.
- Phantom 2: a methacrylate cylinder of 83x100 pixels (height and diameter respectively) with four spherical balls inside of 20 pixels diameter.
- Phantom 3: two set of 8 balls that form two parallel rings mounted on a methacrylate cylinder. Diameter of the ball bearing ring is 70 mm and distance between two rings is 70 mm.

The phantom generator module needs the following input parameters:

- `TYPE_PHANTOM`: It is an integer with the identifier of the selected phantom: 1, 2, 3 for phantom 1, phantom 2 and phantom 3 respectively.
- `DEST`: String with the path for the result file.

The result is a file called 'phantom_`TYPE_PHANTOM'` in the path '`DEST`' with the generated phantom in floats.

3.3.2.Projection module

The projection module simulates the acquisition process producing a set of projections of the input object, with no misalignment or with inclinations (tilt or roll).

The input parameters for the projector, besides the phantom, are the parameters that define the geometry of the system:

- `PHANTOM`: 3D matrix with the volume to project (phantom generated in previous module) in floats.
- `'s','z'`: Integer variable indicating the projection size (*s* and *z in* Figure 3-18)
- `SCAN_ANGLE`: Integer variable with the angle to cover (between 0º and 360º)
- `INIT_ANGLE`: Integer variable with the initial (between 0º and 360º)
- `DIST`: Float variable indicating distance between source and detector in mm

- `BINNING`: Integer from 1 to 4 that determines the pixel size of the image. The pixel size on the detector is 0.4 mm so the pixel size on the image is 0.4/M x *binning* [mm] (where M is the magnification factor, 2 in our case).
- `tilt`: It is an integer data and describes the tilting inclination (in degrees) of the detector.
- `roll`: It is an integer data and describes the rolling inclination (in degrees) of the detector.
- `NUM_PROJ`: Integer indicating the number of projections to be generated. The angle step will be `SCAN_ANGLE/NUM_PROJ`.

The result of the module is a 3D volume of size $[s, z, \theta]$ with the projection for each angle θ.

Supposing a virtual detector placed in the center of the projecting volume, the coordinate system is shown in Figure 3-21:

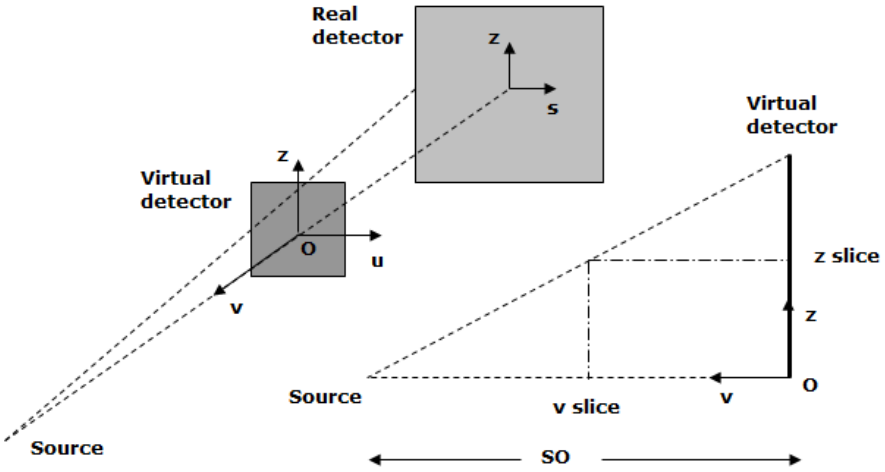

Figure 3-21 Perspective of the simulated cone beam geometry and lateral view (plane v-z) from the virtual detector to the source. The origin is placed in the center of the object (central point in the virtual detector).

z_proy defines the height in the detector where the ray impacts and *z_slice* and *v_slice* are the coordinates of the point in the volume that contributes to this ray.

From Figure 3-21 we have:

$$\frac{z_{\_proy}}{SO} = \frac{z_{\_slice}}{SO - v_{\_slice}} \Rightarrow z_{\_proy} = \frac{SO}{SO - v_{\_slice}} \cdot z_{\_slice}$$

Similarly, *u* coordinate can be calculated:

$$\frac{u_{\_proy}}{SO} = \frac{u_{\_slice}}{SO - v_{\_slice}} \Rightarrow u_{\_proy} = \frac{SO}{SO - v_{\_slice}} \cdot u_{\_slice}$$

The projection module consists on a principal loop that covers the lines of the detector. For each line, it calculates the points in the volume that contribute: fixing the increment in *v*, *u*-index (u_slice) and z-index (z_slice) are calculated from the equations above. Cubic interpolation (INTERPOLATE function in IDL) is used to find the values on these points.

The values are added to the contributions. To obtain projections at different rotation angles the object is rotated (ROT function in IDL).

The inclinations out of the detector plane (tilt and roll in Figure 3-16), are introduced by including an extra step in the projection that finds the correspondence of a point in the ideal projections (with no inclinations) into the real projections. As shown in Figure 3-22, the trajectory of the X-ray along the material is the same in both cases, but the inclination affects to the distance from the center to the point where the ray impacts on the detector plane.

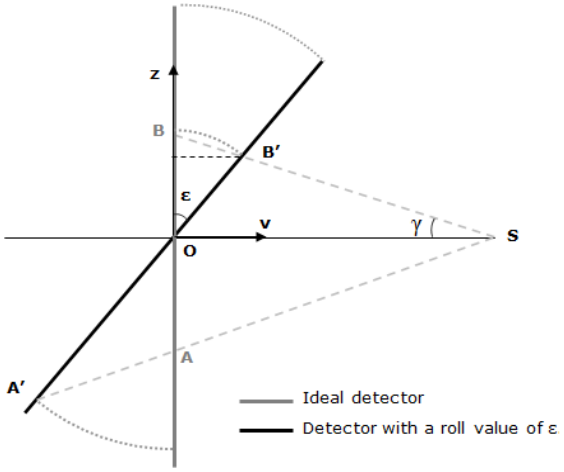

Figure 3-22 Illustration of the ideal and tilted planes where (A', B') are the points of impact of tilted case and (A, B) are the points of the ideal case.

The algorithm calculates the attenuation value for the ideal case (A and B) and then assigns this value to the corresponding point (A' and B') in tilted detector. The transformation from the ideal to the real misaligned projections can be seen as a magnification in each coordinate.

The misaligned coordinate z is given by the following equations:

$$OA = \frac{OA' \cdot cos\varepsilon}{1 + \frac{OA' \cdot sen\varepsilon}{SO}}$$

$$OB = \frac{OB' \cdot cos\varepsilon}{1 - \frac{OB' \cdot sen\varepsilon}{SO}}$$

where the point A is the z-coordinate of the impact of an X-ray in the ideal detector and A' the z-coordinate of the point in the real detector with a tilt/roll of ε.

The projection is not only modified in z-axis but also in s-axis. The algorithm calculates the corresponding s-coordinate in the tilted detector (C' and D') regarding to the ideal case (C and D). It is graphically explained in Figure 3-23.

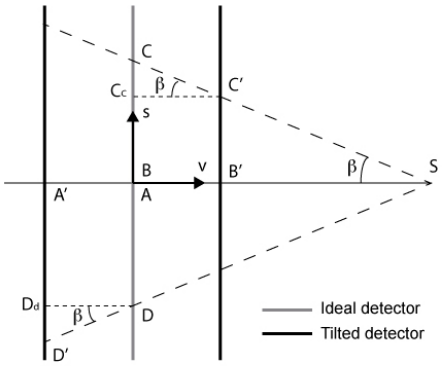

Figure 3-23 Top view of the ideal and tilted plane sections where the points of impact of a ray in a tilted plane are (C', D') and non-tilted (C, D).

The relationship equations in this case are the following:

$$AD = \frac{A'D'}{1 + \frac{1}{SA} \cdot \frac{OA' \cdot sen\varepsilon}{\cos\left(arctg\left(\frac{OA}{SA}\right)\right)}}$$

$$BC = \frac{B'C'}{1 - \frac{1}{SA} \cdot \frac{OB' \cdot sen\varepsilon}{\cos\left(arctg\left(\frac{OB}{SA}\right)\right)}}$$

where the point (C,D) is the s-coordinate of the impact point of an X-ray in the ideal detector and (C',D') the s-coordinate of the point in the real detector with a tilt/roll of ε.

3.3.3. Offset and skew module

The module applies shifts (linear displacements) and skews (rotations) directly to the projection generated by the previous. Translations in X-axis and Y-axis consist on a shift of the 2D projections in multiples of the pixel size, so no interpolation is needed. Skew is introduced by performing a rotation of each projection around the central ray using linear interpolation (function ROT of IDL).

The input parameters of this module are:

- `offset_x`: It is an integer variable that indicates the offset value in x direction (in pixels).
- `offset_y`: It is an integer variable that indicates the offset value in y direction (in pixels).
- `skew`: It is an integer variable with the rotation angle in detector plane (in degrees).

3.4. Characterization of the misalignment effects in the C-arm with the simulator

This section presents the analysis of the effects of the misalignments on both the projections and the reconstructed volume using the simulation tool developed. We study each misalignment independently.

3.4.1.Inclination out of the detector plane

We used Phantom 1 defined in 3.3.1 to study the two types of inclinations of the detector panel around a central axis (vertical for roll, horizontal for tilt). The effect of this misalignment on the projections is the same for both inclinations: elongation of one side and shortening of the other side of the axis (see Figure 3-25). Points further from the axis suffer a bigger deformation.

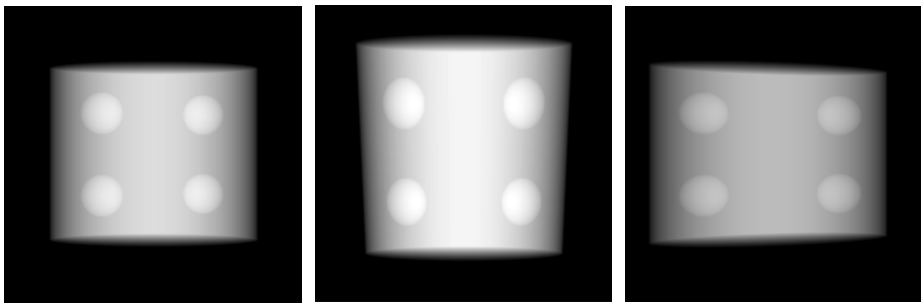

Figure 3-24 Example of projections created when no misalignment is applied (left), and with tilting (center) and rolling (right) inclinations with a value of 30º.

Figure 3-25 shows the effect of these two types of inclinations of the detector panel on the reconstructed image. A tilt of the detector towards the source (as shown in Figure 3-25), produces an elongation and a shortening above and below the central slice respectively (similar to the effect in the projections). The diameter of the balls on the top part of the cylinder (with a tilt of 15º) shows an increase of 10 %. On the other hand, a roll of the detector results in double edges due to the complementary deformation around the vertical axis during the rotation of the scanner.

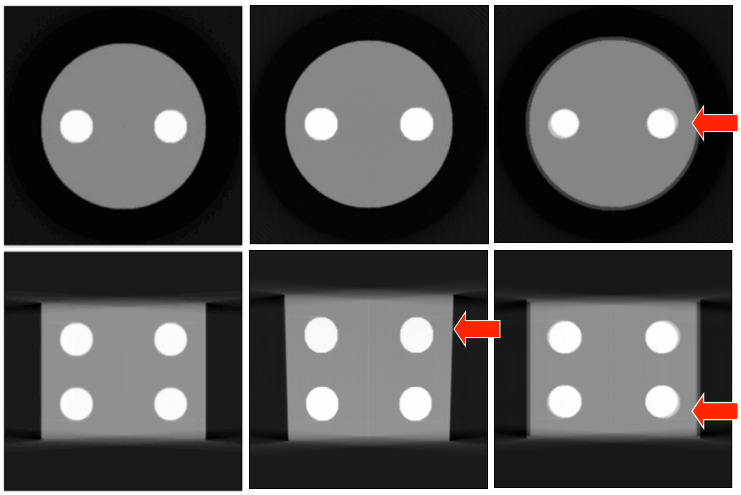

Figure 3-25 Axial (top) and coronal (bottom) views of the phantom for a panel with no inclination (left), with a tilt angle of 20º (middle) and a roll angle of 15º (right).

3.4.2.X-shift and Y-shift

Displacements in the Y direction result in a shift of the whole image but no artifact. A displacement in the X direction shows double edges (for X-shift ≥ 1 pixel). Figure 3-26 shows the effect of X-shift on the reconstructed image.

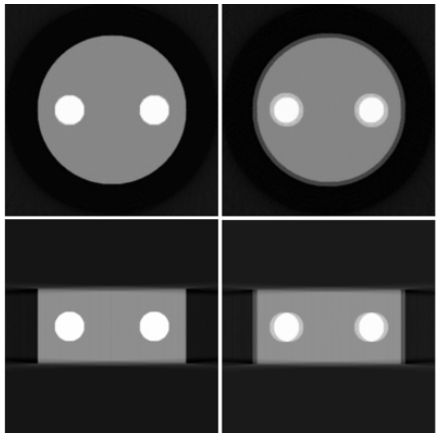

Figure 3-26 Axial and coronal view of the reconstructed image with no misalignments (left) and with 3 pixels in X-offset (right).

3.4.3.Skew

The skew produces artifacts both in the coronal and axial views (except for the central axial slice, shown in Figure 3-27), from values of 1º.

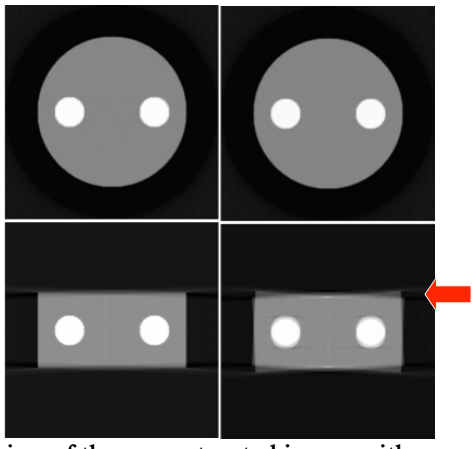

Figure 3-27 Axial and coronal view of the reconstructed image with no misalignments (left) and with a skew of 2.5º (right).

3.4.4.Modification of the source-to-detector distance

To simulate the variation of the distance from source to detector we can do several calls to the Projection module with different values in `DIST`, `INIT_ANGLE`, and `SCAN_ANGLE` each time. In order to evaluate the effect of this variation in the reconstructed image we tested effect of variations of 8% (±*40 mm* from the nominal distance). To this end we build a projection set combining the result of the four following call to the Projection module:

- `INIT_ANGLE=0`, `SCAN_ANGLE` 90º, `DIST` =960 mm
- `INIT_ANGLE=90`, `SCAN_ANGLE` 90º, `DIST` =980 mm
- `INIT_ANGLE=180`, `SCAN_ANGLE` 90º, `DIST` =1020 mm
- `INIT_ANGLE=270`, `SCAN_ANGLE` 90º, `DIST` =1040 mm

Figure 3-28 shows the effect on the reconstructed image of variations of 8% in the source-detector distance during the rotation of the C-arm. We can see artifacts in both axial and coronal views.

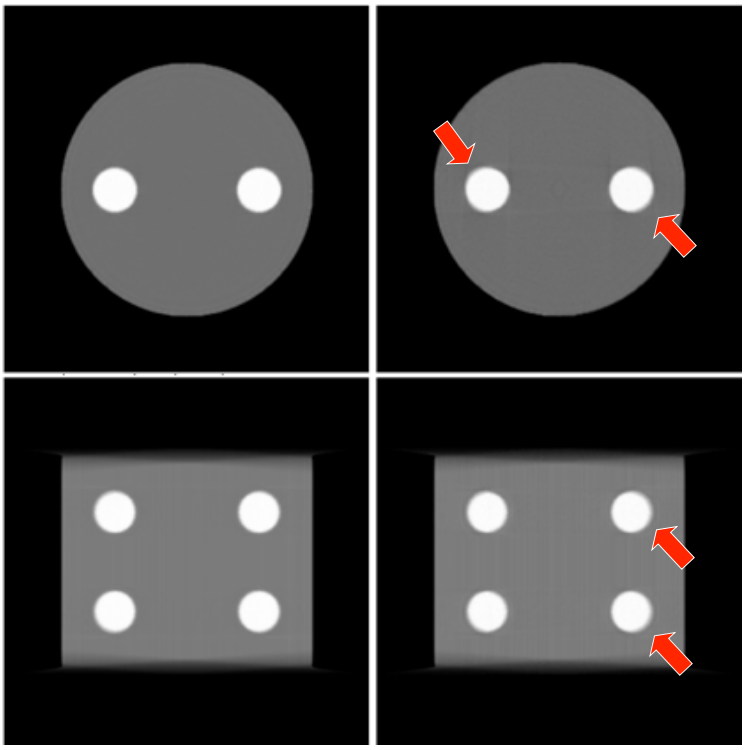

Figure 3-28 Axial and coronal view of the phantom for constant source-detector distance (left) and for a distance variation of ±40 mm (right).

3.4.5. Tolerances

Table 3-1 presents the values corresponding to the different misalignments that a produce noticeable effect on the reconstructed images.

Misalignment	X-shift	Y-shift	Skew	Tilt	Roll	S-D distance
Minimum value that produces visible effects	~0.8mm	-	~1°	~8°	~8°	8%

Table 3-1 Misalignments and corresponding tolerances that produce visible effects on reconstructed images.

4. CALIBRATION

The objective of the geometrical calibration is to characterize the misalignments of the system in order to obtain an accurate image reconstruction from the projection data. Therefore, the principal aim we face in our calibration is the extraction of the data that describes the geometry of our C-arm in order to use as input for the reconstruction program.

As mentioned on 2.4, there are different methods to calibrate an imaging system. Reviewing the literature, we first studied the possibility of using the so called "camera model" calibration based on calculating the projection matrix. Although most geometrical parameters can be calculated from the matrix coefficients, this option was rejected because of the reported instability (Cho et al 2005) and the fact it does not provide the center of rotation as it is focused on projection systems.

The method proposed in (Cho et al 2005) was originally developed for C-arm systems. Geometrical parameters can be estimated at any angular position of the C-arm by using a single projection of a simple phantom allowing the calibration of arbitrarily complex trajectories in cone-beam CT acquisitions. In (Daly et al 2008) the authors used this method to perform a calibration of a C-arm system. For this reasons, this method was selected adapting the dimensions of the phantom to the characteristics of our system.

This method consists on a general analytic algorithm for estimating the geometric parameters that describe the geometry of a cone beam system. According to the authors, the calibration parameters that can be obtained with this method are the following: detector rotation (skew), inclination angles (tilt and roll), piercing point location (projection of the world coordinate origin), SDD (source to detector distance) and source position. These parameters are enough to have a complete description of the geometry of the system.

In this section we describe the implementation of the calibration method only for obtaining linear shifts and skew of the detector as these are the geometrical misalignments more susceptible of introducing artifacts on reconstructions as discussed on section 3.3. We assume tilt and roll equal to zero given that the results of the simulations explained in the previous chapter showed a larger tolerance to these misalignments. We also present the procedure to perform the estimation of inclination angles and source position (in appendix C), as information to take into account in future works.

4.1. System geometry

The phantom used by the method consists on two rings formed by ball bearings mounted on a cylinder in order to be symmetric between them. The origin of the world coordinate system is located at the center of the circular pattern of the calibration phantom in the x and y directions and in the middle of the two circular patterns in the z direction (Figure 4-1).

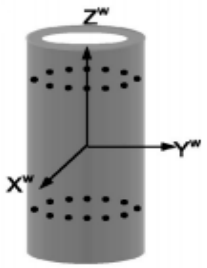

Figure 4-1 Illustration of the phantom and origin of world coordinate system.

Geometry of the system is defined by three different coordinate systems: the coordinate systems of the world (*w*), virtual detector (*i*) and real detector (*I*). The world coordinate system (x^w, y^w, z^w) is fixed to the calibration phantom. The virtual detector coordinate system (x^i, y^i, z^i) is used when detector is perfectly aligned. And real detector coordinate system (x^I, y^I, z^I) models the possible inclinations (ϕ, θ) and rotation (η) of the detector from the virtual detector plane (Figure 4-2).

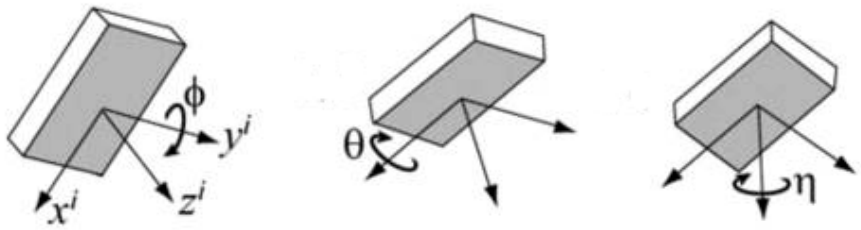

Figure 4-2 Illustration of detector tilt and rotation angles applied on the virtual detector coordinate system (*I*, shown in the left) to produce the real detector coordinate system (*I*, not shown in the picture).

An illustration of the coordinate systems and their origin is shown in Figure 4-3.

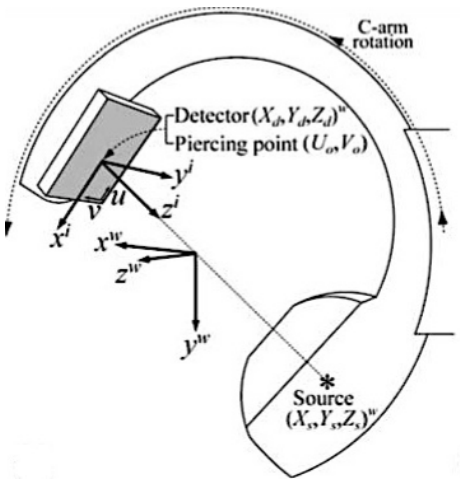

Figure 4-3 System geometry of the cone-beam C-arm. The positions of the source (X_S,Y_S,Z_S) and detector (X_d,Y_d,Z_d) with respect to the world coordinate system are shown.

The position of the source and detector are denoted $(X_S, Y_S, Z_S)^w$ and $(X_d, Y_d, Z_d)^w$, respectively. Both the virtual and real detector coordinate systems have their origin at the piercing point (U_0,V_0) (see Figure 4-3). The piercing point is the projection of the origin of the world coordinate system on the detector plane.

The coordinate axes are denoted using lower case letters (e.g. x^w) and coordinates of a specific object are denoted using upper case letters (X_d).

The z axis of the world coordinate system (z^w) points along the rotation axis of the C-arm gantry, y^w axis points to the source at a gantry angle of 0º, and the x^w axis points to the source at a gantry angle of 90º (Figure 4-3). The directions of the axes of the coordinates on the detector coordinate system are also defined on Figure 4-3.

Summarizing, the geometry of the C-arm is characterized by the following 12 system parameters:

- Detector rotation: ϕ, θ, η
- Piercing point location: U_0, V_0
- Gantry angle: γ
- Source position: X_S, Y_S, Z_S
- Detector position: X_d, Y_d, Z_d

These parameters can be reduced to nine degrees of freedom by characterizing the detector position specifying the source-to-detector distance (SDD) and calculating the gantry angle based on the source position.

So, taking this into account, the needed parameters are:

- Detector rotation: ϕ, θ, η
- Piercing point location: U_0, V_0
- Source-to-detector distance (SDD)
- Source position: X_S, Y_S, Z_S

The geometrical parameters resulting from the calibration are determined with respect to the world coordinate system attached to the phantom.

4.2. Determination of calibration parameters

4.2.1. Piercing point

Lines in space are projected into lines on a detector if it is flat. An intersection of lines is also projected as intersection. As shown in Figure 4-4, the piercing point is defined by the intersection of all the lines connecting opposite balls from the two circular patterns (which are ellipses in the projection). Therefore, the piercing point can be calculated finding the intersection of the lines projected in the detector plane.

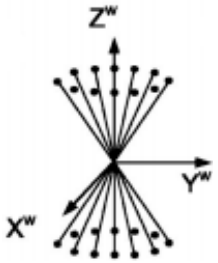

Figure 4-4 Illustration of balls and corresponding lines for piercing point calculation.

4.2.2.Rotation of the detector (η)

The rotation of the detector with respect to its normal axis is referred as η. Estimation of the rotation of the detector makes use of the common features of the projected elliptical patterns. The two points corresponding to the extremes of the projected ellipse form the lines L_1 and L_2 (Figure 4-6) Note that the location of these extremes is found from the numerical model of the ellipse and not directly from the projection of the balls.

Intermediate axis α and β are used in some figures and explanations. These are illustrated in the Figure 4-5 below:

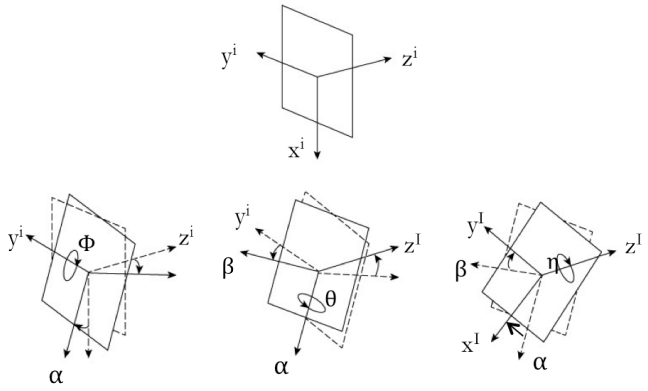

Figure 4-5 Illustration of the nomenclature of the axis after movements on the detector. Index *i* represents virtual detector coordinates, index *I* represents real detector coordinates and α and β the intermediate axis.

The projection image of a hypothetical ring of balls in the phantom shown as broken circle is a simple line passing through point P_a (length of the short axis is zero). Since the line passing through P_a is always parallel to axis α, the angle between this line and X^i is the same as the detector angle η. As seen on the Figure 4-6, the line L_a is parallel to the lines L_1 and L_2 when ϕ is zero.

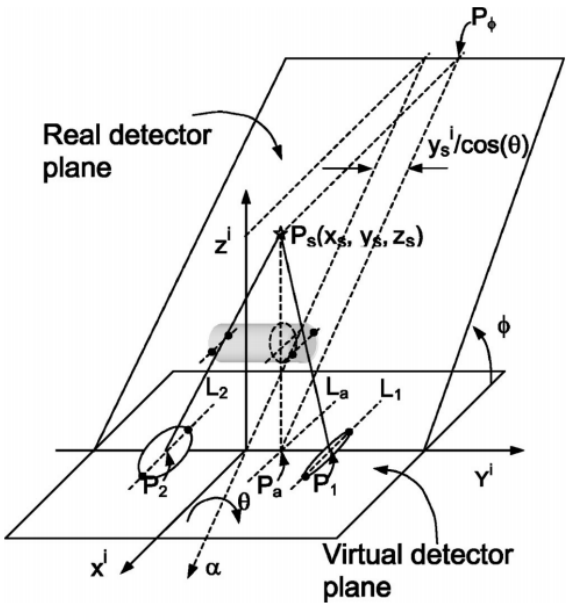

Figure 4-6 Illustration of lines L_a, L_1 and L_2 on the virtual detector plane. α axis is shown in the figure.

First of all, the location of P_a must be calculated by using the equation that relates the ratio of short axis to long axis of the ellipses ($\sqrt{a_k/b_k}, k = 1,2$) with the distance from the point P_a to the center of each ellipse P_1 and P_2.

$$\frac{P_2^a}{P_a^1} = \frac{P_0^a - P_0^2}{P_0^1 - P_0^a} = \frac{\sqrt{a_2/b_2}}{\sqrt{a_1/b_1}}$$

$$P_0^a = \frac{(P_0^1\sqrt{a_1/b_1} + P_0^2\sqrt{a_2/b_2})}{\sqrt{a_1/b_1} + \sqrt{a_2/b_2}}$$

where P_m^n is a position vector from point *m* to *n*.

The angles of lines L_1 and L_2 with respect to L_a are proportional to the distances from P_1 and P_2 with P_a. When the detector rotation angle η is not zero the following relation can be used.

$$\frac{P_2^a}{P_a^1} = \frac{A(\alpha, L_2)}{A(\alpha, L_1)} = \frac{[A(X^I, L_2) - \eta]}{[A(X^I, L_1) - \eta]}$$

therefore rotation is obtained by the following equation:

$$\eta = \frac{[P_a^1 \cdot A(X^I, L_2) + P_2^a \cdot A(X^I, L_2)]}{P_1^2}$$

4.3. Calibration workflow

The calibration algorithm follows four steps:

1) Once projections of the calibration phantom have been acquired, the program **segments the balls** in order to isolate them and work easier with them. Figure 4-7 shows an example of resulting projections.

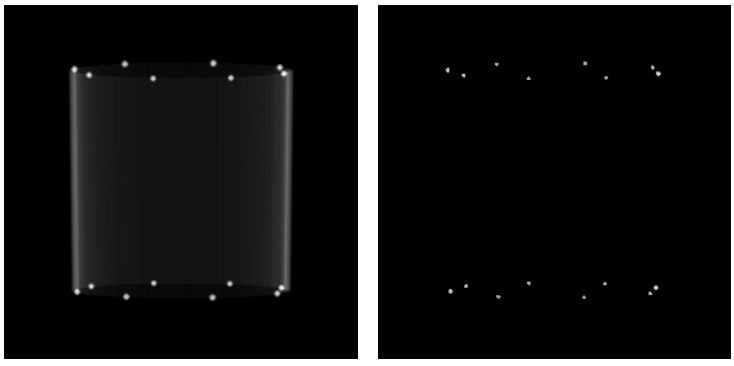

Figure 4-7 Example of simulated projections (with no misalignment included). Image on the left shows projection before segmentation of the balls. Image on the right shows the same projection with segmented balls.

2) **Obtaining the position of the balls** is the next stage on the procedure. A threshold to identify the edges of each ball bearing and a numerical optimization function in

Matlab is used to find the center of each ball bearing. The program used in this step is taken from camera model calibration software developed together with the UPM in 2012.

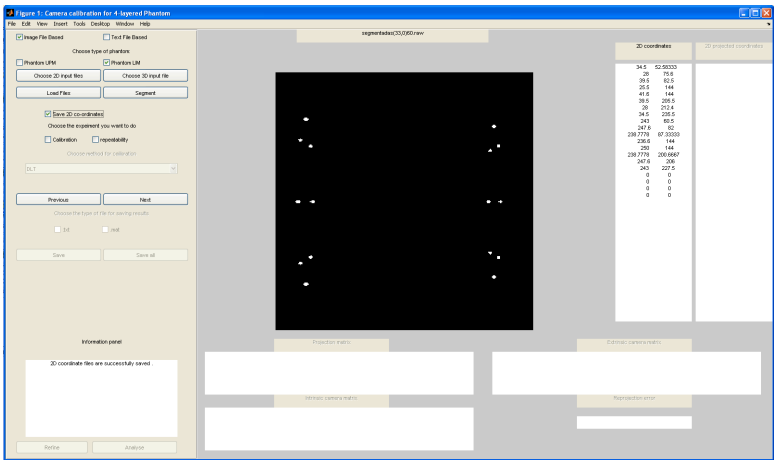

Figure 4-8 Screenshot of the program that finds the position of the balls on the image.

Consideration of the coordinate axis position and directions used by the different programs must be done carefully to avoid problems with positioning. As shown in Figure 4-8 and regarding to the coordinates identified by the program, a relationship between coordinates used by this program and the ones considered in the calibration method must be done. Below, a graphic explanation of the problem is shown in Figure 4-9. The solution is simple and consists on an easy coordinate change.

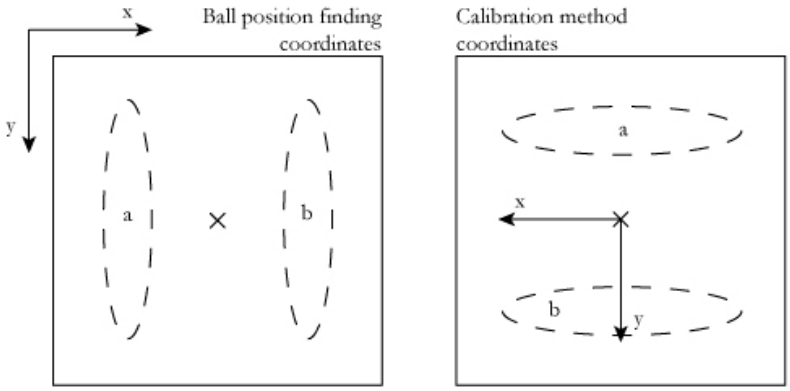

Figure 4-9 Coordinates position and directions in both systems: the one used by the ball position finder program and the one considered in the calibration method. Notice that the program displays the image in the left rotated 90º (ellipses appear identified as *a* and *b*).

Obtaining the proper coordinates of each ball bearing projection allows us to use them in the calibration method, directly or by identifying the ellipse formed by the whole set of ball projections.

3) **Adjusting the ellipse to the coordinates** of the projection of the balls is necessary. The calibration method makes use of the formed ellipses parameters such as magnitude of major and minor axis and rotation value.

Based on the method proposed on (Noo *et al* 2000), a program in *Matlab* extracts the parameters needed out of the list of ball projection coordinates obtained before. Apart from major and minor axis magnitude and rotation values, the program defines the ellipse with the equation used in the calibration method shown in ELLIPSE MODEL EXPLANATION above.

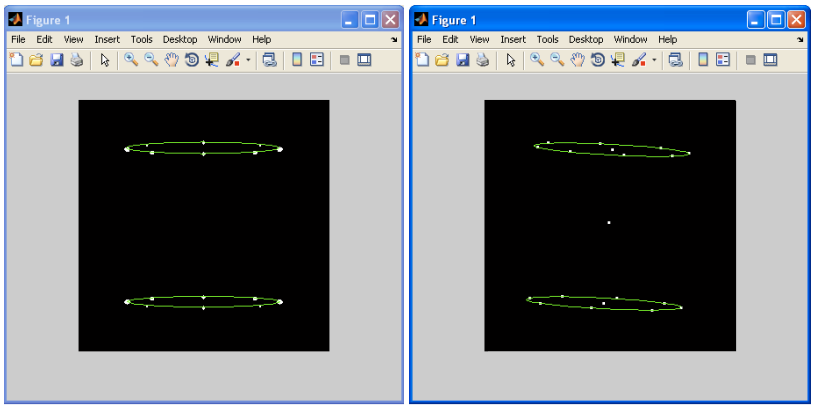

Figure 4-10 Examples of simulated projections. Adjusted ellipse is displayed on both images with (left) and without (right) rotation.

4) Finally, once the coordinates of balls projections and ellipse parameters are obtained, an **algorithm in *Matlab* follows the procedure described by the calibration method** to estimate the calibration parameters (piercing point and skew in this case).

4.4. Evaluation of the calibration algorithm

To evaluate the calibration tool we used simulations of Phantom 3 defined in (3.3.1) using the phantom creation module. We simulated projections with shifts and rotation using projection and offset and skew modules described in 3.3.

A chart with offset values tested is shown below. These results are obtained by calculating the piercing point location for projections simulated with no displacement applied.

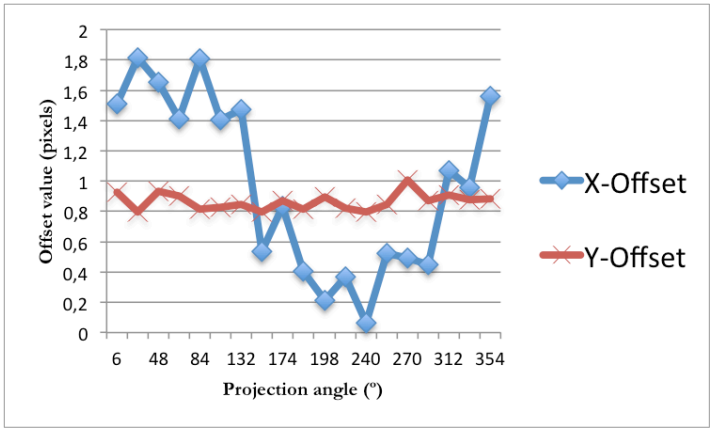

Figure 4-11 X-offset (blue) and Y-offset (red) values for some projection angles between 0º and 360º.

When applying displacements in the projections, original offset values remain constant (for both positive and negative displacements). This means that the error in the estimation of the piercing point identified with centered projections, though variable as seen on Figure 4-11, remain constant when applying displacements.

Errors in the estimation for simulated rotation values are shown in Figure 4-12. In the sample with 14 projections, variability is appreciated and three values present errors above 3%.

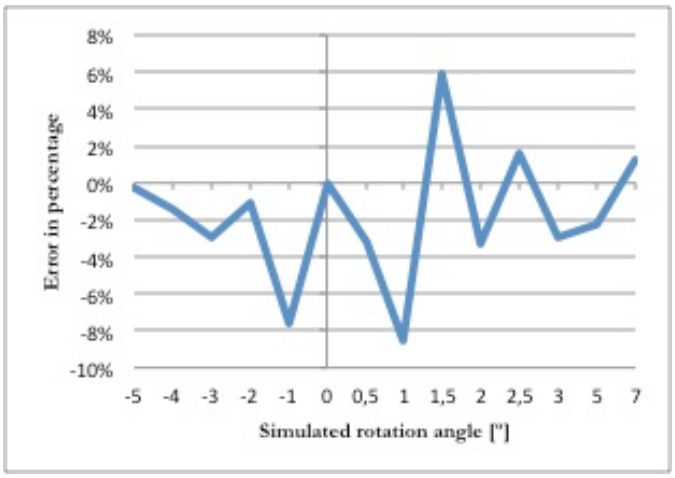

Figure 4-12 Error in the estimation of rotation angle for different simulated values.

4.5. Calibration phantom

The work in Daly et al. (Daly et al 2008) makes use of a calibration phantom consisting of 16 ball bearings in a known geometry. Eight balls are spaced evenly at 45º in two plane-parallel circles separated by a given distance along a cylindrical plastic tube (Figure 4-13). The diameter of each ball bearing is 4.7 mm, the diameter of each circular pattern is 100 mm and the distance between the two parallel circles is 90 mm. Alternative sizes of bearings and number of balls can be supported with appropriate adjustments to constants in the algorithm. The authors of the algorithm claim that more than ten ball bearings (five in each circle) should be used in the design of an appropriate calibration phantom in order to obtain a good correspondence with an ellipse pattern on the projections. The positions of the balls in both circles are symmetric regarding to the central section plane, as it is clearly shown on Figure 4-1.

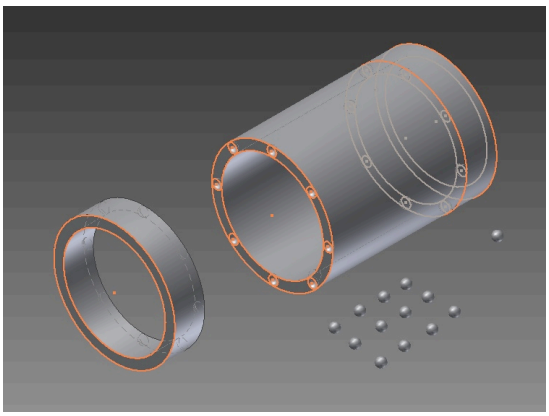

Figure 4-13 Drawing of the phantom (with two covers to protect the balls, not included in final version).

The calibration phantom is dimensioned to cover most of the detector, which in the case of the study performed in (Daly *et al*) is a flat panel detector with dimensions 40×30 cm. In order to adapt the phantom to the characteristics of our equipment we changed its dimensions, taking into account the 23 cm diameter of the image intensifier (11.5 cm diameter field of view) (see Figure 4-14).

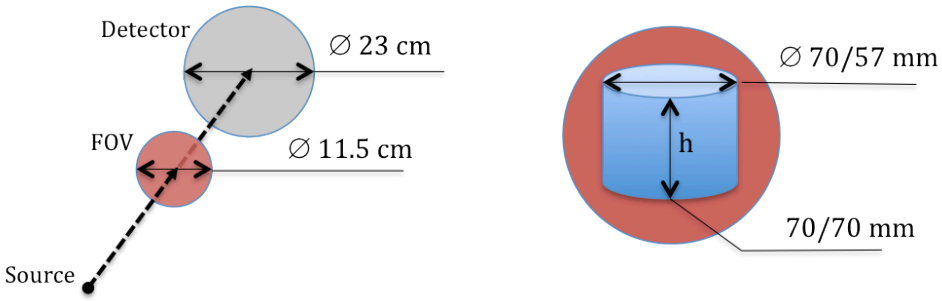

Figure 4-14 Illustration of the dimensions of the detector and the FOV of our system (left) and the phantom dimensioned to cover most of the FOV (right).

We built two different phantoms with similar characteristics. The first one consists on a methacrylate tube of 3 mm thick with 16 cavities drilled on each end of the tube to use more ball bearings if necessary. The diameter of each circular pattern is 70 mm and distance between two parallel circles is 70 mm. The diameter of each ball bearing is chosen to be large enough to include a large number of pixels, but small enough to minimize overlapping with neighboring balls in projections. We chose a ball bearing diameter of 2 mm diameter to adapt it to the new dimensions. The second one has 3 mm ball bearings mounted on a 4 mm thick methacrylate tube. The diameter of the circular pattern is 57 mm and distance between parallel circles is 70 mm (Figure 4-15). We decided to build two phantoms in order to evaluate which one is the optimum option when using it with the calibration algorithm. Table 4-1 summarizes the dimensions of the phantoms:

	DETECTOR SIZE	∅ of the circular pattern (mm)	Distance between two circles (mm)	∅ of the balls (mm)
Daly et al.	**40x30 cm**	**100**	**90**	**4.7**
Phantom 1	**∅ 23 cm**	**70**	**70**	**2**
Phantom 2	**∅ 23 cm**	**57**	**70**	**3**

Table 4-1 Phantom dimensions for the case on the literature and our case, regarding to the detector size

Both phantoms were produced at the Technique Office at Carlos III University in Madrid. The final version of the phantoms has no covers at the ends; instead, an adhesive tape is used to hold the get the balls attached (Figure 4-15).

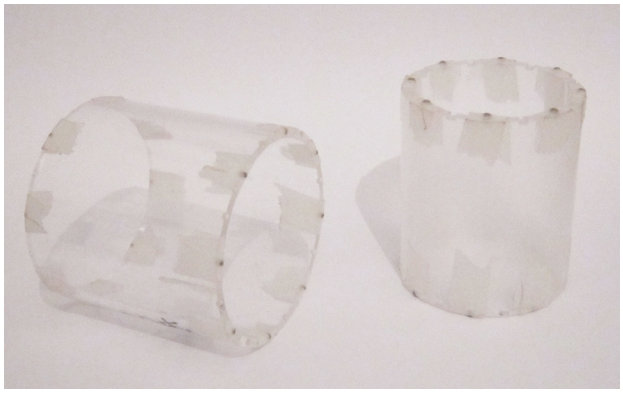

Figure 4-15 Photograph of the two phantoms built. The one with 70 mm diameter circular pattern and 2 mm ball bearings (left) and 57 mm diameter circular pattern and 3 mm ball bearing (right).

In order to have the calibration phantom visible in all projections, it must be placed approximately near the nominal center of the field of view the system and with its longitudinal direction aligned roughly to the axis of rotation (see Figure 4-16). Since all measurements are referenced to the phantom, it is not necessary to place the phantom with great accuracy in the world coordinate system.

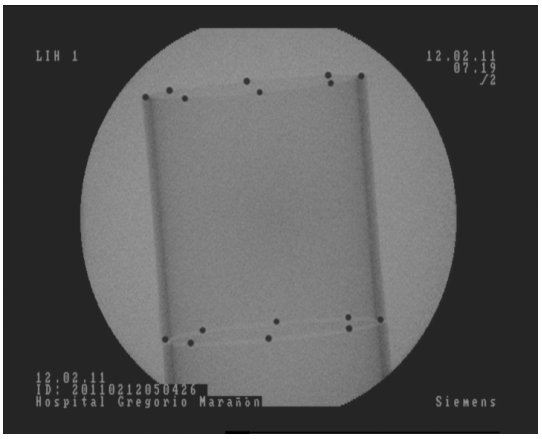

Figure 4-16 This image from a real acquisition of the C-arm in the laboratory shows that the phantom designed fits perfectly in the FOV. Rotating the C-arm around the phantom must be done carefully as outer balls are near the limits of the FOV.

We took 192 projections covering 360 degrees around the calibration phantom with the C-arm following the angulation movement. The angular position was monitored by attaching an inclinometer to the case and taking measurements for each projection (Figure 4-17).

Figure 4-17 Photographs of the acquisition made around the calibration phantom (left) with an inclinometer attached to measure the angular position (center and right).

5. DISCUSSION AND CONCLUSSIONS

This thesis, within the framework of a line of research on IORT, has focused on the problem of using a C-arm to obtain tomographic images, exploring the possibility of obtaining images of the patient after surgery to perform a better planning of the therapy.

First of all, an evaluation of the sources of errors including distortion in the image intensifier, stability and repeatability of the acquired images and geometrical misalignments was done, based on acquisition of different phantoms. Our results showed that distortion was not an issue in our image intensifier and stability of intensity values was good (changes under 1 %). As for geometrical repeatability, projections acquired for same angular positions in acquisitions taken along a period of time without moving the C-arm showed no difference, but when these acquisitions were taken after intermediate movements variations were appreciated. This could indicate looseness somewhere in the physical part of the system but the most probable explanation is the fact that the phantoms used were all attached to the case of the detector and this may not be completely rigid. We contacted the SIEMENS technical support office and they suggested that behavior of the inner structure of the C-arm (arc where the source and detector are mounted) was rigid and that the looseness should be in the case that protects the detector. Placing the phantoms attached to the case is therefore a source of error that could be giving wrong information about functioning of the source-detector system.

Regarding the repeatability for projections at different angular positions, when acquiring images at different orbital positions (without varying the angulation) results were more stable. This is most likely due to the fact that the C-arm is more resistant to deformations on the vertical plane (perpendicular to the floor). In fact, C-arm systems normally make use of the orbital movement to get a good positioning regarding to the patient. The problem is that the orbital movement has a rotation limitation of 130º, not allowing obtaining projections covering 360 degrees, which are ideally used for image reconstruction. In contrast, the more unstable movement (angulation) allows a complete 360º rotation around the patient.

From these results we conclude that the possibility of reconstruction using only a limited angle of 130º should be studied. Also, the fact that projections differ for different angular positions indicating that non-idealities are not constant indicates the need of performing a geometrical calibration of the system for the whole geometric space covered by the C-arm. An option could be performing a calibration for some angular positions and estimating by interpolation the parameters for intermediate values.

Regarding geometrical misalignments, we developed a software tool that emulates the acquisition process in the C-arm making possible the inclusion of geometrical misalignments, to evaluate the effect of each of the possible sources of error of this type on both projections and reconstructed images. Our results showed that a careful calibration skew and X-shift is advisable since small errors in this parameters result in very conspicuous artifacts on the reconstructed images. The tolerance to tilt and roll misalignment was found to be larger, for values that might not be present in the scanner. Deformations of the arc during rotation of 8% (±4 cm) will also result in artifacts, indicating that the calibration of the distance source-detector should be done for each angular position.

In this study, the error sources are introduced with constant values. This means that the system misalignments remain constant, presenting same values for any angular position of the arm.

Apparently it does not reproduce the real case, the effects with variable misalignments should be evaluated.

A first implementation of the algorithm has been done, for the estimation of the rotation and translation on the detector, which are the error sources more susceptible of introducing artifacts in the image.

6. FUTURE WORK

Given that the work done in this thesis is just the first step towards the final goal of obtaining tomographic images from a C-arm system, the future work is extensive.

The first thing to do will be to improve the calibration software to be able to obtain a complete geometrical description of the system including the calculation of tilt and roll angles of the detector. Besides, it would be interesting to do a more careful evaluation and try to minimize the errors in the misalignment parameters.

The next step will be to perform the calibration algorithm with real acquisitions of the designed phantom.

We will need also to evaluate the stability of the calibration parameters; if they are stable enough in time for each position, calibration will be valid for a reasonable period and will not be necessary very often. So obtaining different acquisitions of the calibration phantom and comparing the results will be essential.

With the goal of obtaining tomographic images with the C-arm, a very important task is the evaluation of the optimum acquisition protocol. This will consist on studying how many projections and from which angles are optimal. Taking into account that the movements are done manually, fewer projections lead to an easier and faster acquisition procedure but a minimum number of projections are needed to achieve a good quality reconstruction. A simulator like the one developed would be a good tool to carry out this study.

Finally, we will need to evolve the reconstruction software available so that it can work with non-equidistant projections resulting on an acceptable image quality.

7. BUDGET

In this chapter the global costs of the realization of this project are presented. Personnel costs and material costs are treated separately.

- PERSONNEL COSTS

The project has been developed following a model structured in seven phases steps that have associated tasks described below. Time assigned to each one of the tasks is estimated in weeks. Each working week corresponds to 40 hours.

1. Requirement determination phase

This phase includes the definition of the objectives of the project and the determination of the tasks involved to achieve them.

Estimated time: 1'5 week

2. Preliminary research phase

In order to acquire the necessary knowledge to develop the work and use the specific tools some tasks were carried out.

- Initial contact with the used image technique (X-rays).
- Approach to the contextual frame where the project belongs.
- Installation of the tools needed to develop the algorithms.
- Initial contact with the programming language used to implement the algorithms.
- Study of the functioning of the C-arm equipment.
- Study of the concepts of tomographic image reconstruction with X-rays.
- First approach to the behavior of the equipment and preliminary studies of the non-idealities by the study of real projections.

Estimated time: 8 weeks

3. Simulator designing phase

This phase includes all tasks related to the evaluation of misalignment effects tools.

- Study and adaptation of the projections simulator to the characteristics of our system.
- Study and adaptation of the misalignment simulator tool.
- Study of the reconstruction algorithm and adaptation to simulator images.
- Implementation of the misalignment simulation tool and interpretation of the images obtained.

Estimated time: 8 weeks

4. Camera calibration method developing phase

Together with the *Universidad Politécnica de Madrid*, our imaging group was developing a calibration method based on the camera model before this project started. In order to evaluate the possibility of using this method to calibrate our system, a study and development of software was done. This phase includes the study of the advances achieved in the matter and the subsequent work on it.

- Studying of the used camera model calibration method.
- Approach to the calibration algorithm developed in UPM.
- Analysis of the application possibilities of the method regarding to the actual problems of the equipment and the final objectives of the project.
- Adaptation of the algorithms and tools developed in UPM to be useful for our equipment and specifications.
- Analysis of the data obtained.

Estimated time: 3 weeks

5. C-arm calibration method implementation phase

Understanding, adaptation and implementation of the tomograph calibration method proposed by *Cho et al.* is the main objective of this phase.

- Analysis and study of the bibliography concerning to the calibration objective.
- Understanding of the concepts used in work of *Cho et al.* and its possibility of adaptation to our specific case.
- Designing of the phantoms to use in our C-arm calibration.
- Adapting the misalignment simulation tool to make projections imitating the acquisitions of the C-arm of the calibration phantom.
- Adapting the ball segmentation program designed in UPM to work with the calibration phantom simulated images.
- Developing of an ellipse modeling algorithm in *Matlab* in order to obtain the parameters describing the ellipses formed by ball bearing in projections.
- Writing down the calibration algorithm in *Matlab*, adapting it to the characteristics of our system.

Estimated time: 10 weeks

6. Project report development phase

In this last phase of the project the report is developed, where all the work done, conclusions and future work are presented.

Estimated time: 9'5 weeks

All this information is summarized in Table 7-1:

PROJECT PHASE	DURATION (weeks)
1. Requirement determination phase	1'5
2. Preliminary research phase	8
3. Simulator designing phase	8
4. Camera calibration method developing phase	3
5. C-arm calibration method implementation phase	10
6. Project report development phase	9'5
TOTAL TIME ESTIMATION	**43**

Table 7-1 Project phases and time used estimation.

Therefore, total time estimation (in hours) is the following:

Total time estimation: 43 weeks → 1720 hours

Taking into account the salary for an engineer comes to 25 €/hour, the total personnel costs associated to the development of the project is:

Total personnel cost: 43.000 €

- MATERIAL COSTS

Below the costs of used material in the realization of the project are shown:

Material used	Cost	% time spent in the project	Dedication (months)	Depreciation time (months)	Allocable cost (€)
Personal computer. Intel core i7 processor, 4-cores, 8GB RAM	1500 €	100%	10	60	250
IDL programming language license	300 €	100%	10	60	50
Matlab programming language license	6000 €	100%	10	60	1000
				TOTAL	**1300 €**

Table 7-2 Cost of used material.

- **TOTAL ECONOMIC COST**

From the obtained results of costs including personnel and material, final budget is calculated taking into account the 21% VAT:

CONCEPT	COST (€)
Personnel costs	43000
Material costs	1300
Sum of both costs	44300
VAT (21%)	9303
TOTAL	**53603 €**

Table 7-3 Final budget of the project.

Therefore, the **total budget** of this project comes up to:

Total budget: 53.603 €

8. APPENDIX

A. SCIENTIFIC PUBLICATION DERIVED FROM THIS THESIS

From M. Paraíso, C. de Molina, J. Pascau, M. Desco, M. Abella. *Evaluation of the effect of calibration accuracy in a C-arm for its use in tomography*. Poster in the XXX Annual Conference of the Spanish Society for Biomedical Engineering CASEIB, San Sebastián, 2012.

Evaluation of the effect of calibration accuracy in a C-arm for its use in tomography

M. Paraíso[1], C. de Molina[2], J. Pascau[2], M. Desco[1,2,3], M. Abella[2]

[1] *Instituto de Investigación Sanitaria Gregorio Marañón, Madrid*

[2] *Departamento de Bioingeniería e Ingeniería Aeroespacial, Universidad Carlos III de Madrid*

[3] *CIBER en Salud Mental (CIBERSAM), Madrid*

1.Introduction

Context of the study: *radiance* project

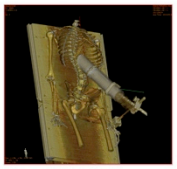

- Intraoperative Radiation Therapy (IORT) treatment is the irradiation of post-resected tumor beds during surgery
- Planning of external radiation therapy parameters (dose, volume choice…) is done on a previous CT
- Our group has developed a radiation therapy planning tool, introducing concepts from external radiotherapy in IORT
- Anatomy changes during surgery

OPTION: to use a C-Arm as a tomograph to obtain 3D images of the patient during IORT

C-arm equipment

- Designed to obtain planar images, it offers a wide variety of movements

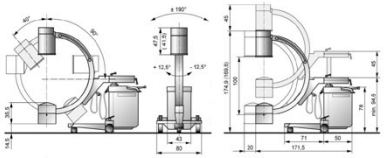

- C-Arm working as a tomograph will be analog to a CT scanner with cone-beam geometry
- Mechanical strains and looseness in the detector and the movements that differ from a circular path cause misalignments on the projections

OBJECTIVE OF THE WORK: Evaluation of the effects of these non-idealities in reconstructed images for its use as a tomograph

2.Misalignment simulator tool

- Implemented using IDL 6.4, the tool emulates the acquisition in a C-arm system: it produces a set of projections of synthetic phantoms based on the parameters that describe the real system
- It includes inclinations out of the detector plane (roll and tilt), rotation (skew) and translation in X and Y of the panel detector
  - Skew and offsets are introduced after projection using rotations and shifts
  - Tilts are included during projection: extra step finding the correspondence of a point in the ideal projections (with no inclinations) into the real projections

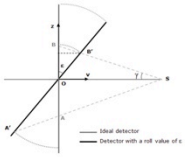

$$OA = \left(1 - |tg\gamma| \cdot |\sin\varepsilon|\right) \cdot |\cos\varepsilon| \cdot OA'$$

$$OB = \left(|\cos\varepsilon| + |\sin\varepsilon| \cdot |tg\gamma|\right) \cdot OB'$$

- Experiments based in the C-arm available at the lab: *SIREMOBIL Compact L.* Siemens

GEOMETRY OF THE SYSTEM:

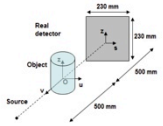

PHANTOMS:

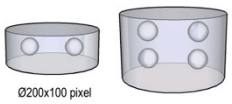

Ø200x100 pixel

Ø200x166 pixel

3.Results

MOVEMENTS ON THE DETECTOR PLANE

Image with no misalignments

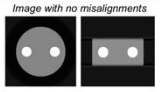

Linear shifts

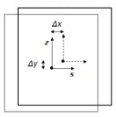

Displacements in Y direction result in a shift of the whole image but no artifact

Shifts in X direction show double edges (3 pixel X-offset in figure)

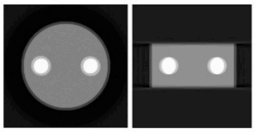

Skew

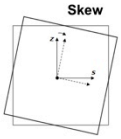

Skew produces artifacts both in the coronal and axial views (skew angle of 2.5 º shown in figure)

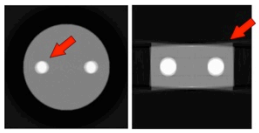

INCLINATIONS OUT OF THE DETECTOR PLANE

Image with no misalignments

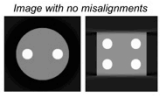

Projections suffer elongation of one side and shortening of the other side of the axis

Tilt

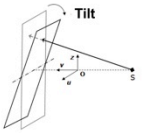

The length of the balls on the top part of the cylinder increases a 10 % for tilting value of 15º

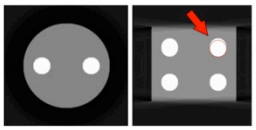

Roll

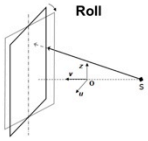

Double edges due to the complementary deformations with roll angle of 15º

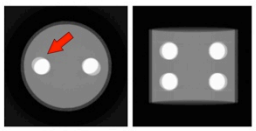

CHANGES IN SOURCE-DETECTOR DISTANCE DUE TO DEFORMATIONS OF THE ARM

Image with no misalignments

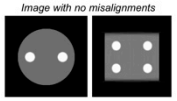

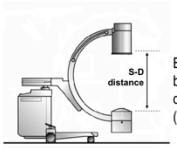

Blurry edges at sides of the balls in coronal views with a distance variation of ±40 mm (8% of the nominal distance)

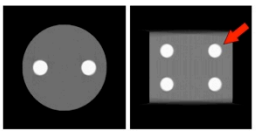

MISALIGNMENTS AND CORRESPONDING TOLERANCES

Misalignment	X-shift	Y-shift	Skew	Tilt	Roll	S-D distance
Minimum value that produces visible effects	~0.8mm	-	~1º	~8º	~8º	8%

4.Discussion and conclusions

- A careful calibration of skew and X-shift is advisable since small errors in these parameters result in very conspicuous artifacts
- Tilt and roll misalignment reduce the quality of the images for large misalignment values
- Small deformations of the arc during rotation will result in artifacts, so a calibration of the distance source-detector should be done for each angular position
- Future work will include the development of a calibration algorithm taking into account these results and experiments with real data from the C-arm

Acknowledgements

This work was partially funded by AMIT project (CEN-20101014) from the CDTI-CENIT program, RECAVA-RETIC Network (RD09/0077/00087), projects TEC2010-21619-C04-01 and TEC2011-28972-C02-01 from Spanish Ministerio de Ciencia e Innovación, ARTEMIS program (S2009/DPI-1802) from Spanish Comunidad de Madrid, and IPT-300000-2010-003. INNPACTO from Ministerio de Ciencia e Innovación

B. GENERAL VIEW OF THE C-ARM SYSTEM

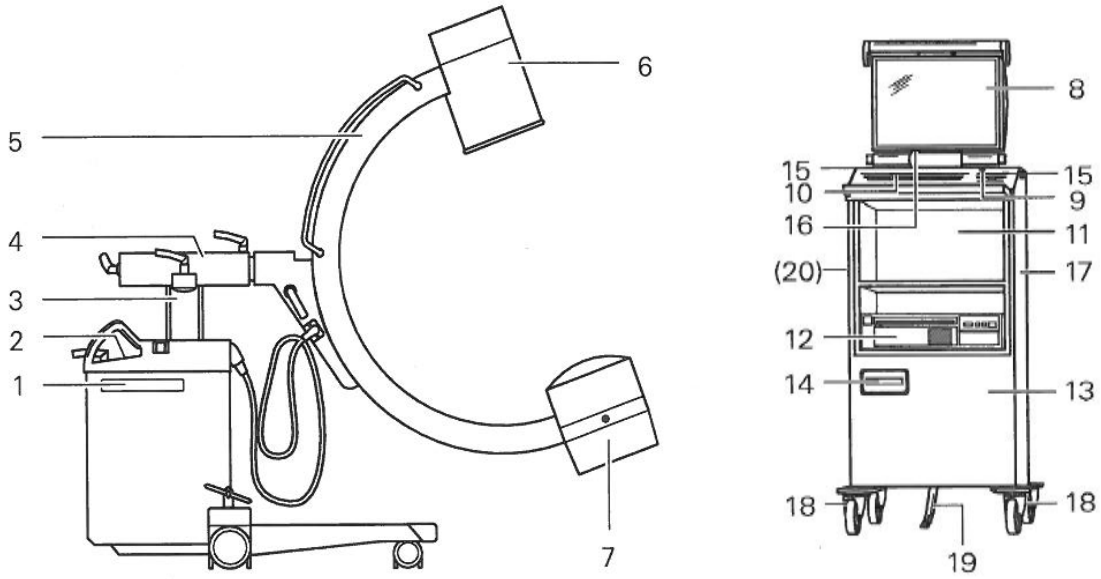

(1) SIREMOBIL electronic unit
(2) Control panel
(3) Elevation column
(4) Horizontal support arm
(5) C-arm
(6) Image intensifier with integrated TV camera
(7) Monobloc tube with X-ray emitter and integrated collimator.
(8) Monitor
(9) Connection/disconnection switch
(10) Keyboard
(11), (12) Compartiment for storage or space for printer
(13) Monitor cart
(14) MOD unity (optional)
(15) Radiation indicator
(16) Ambient light sensor
(17) Frontal handle
(18) Multi-directional wheels
(19) Earth-connecting strip
(20) Cable holder (not visible in the figure)

General view of the screen and control elements:

Control panel and screen area for making the examinations are located in the C-arm system.

Different keys and screens are grouped in specific areas depending on their function.

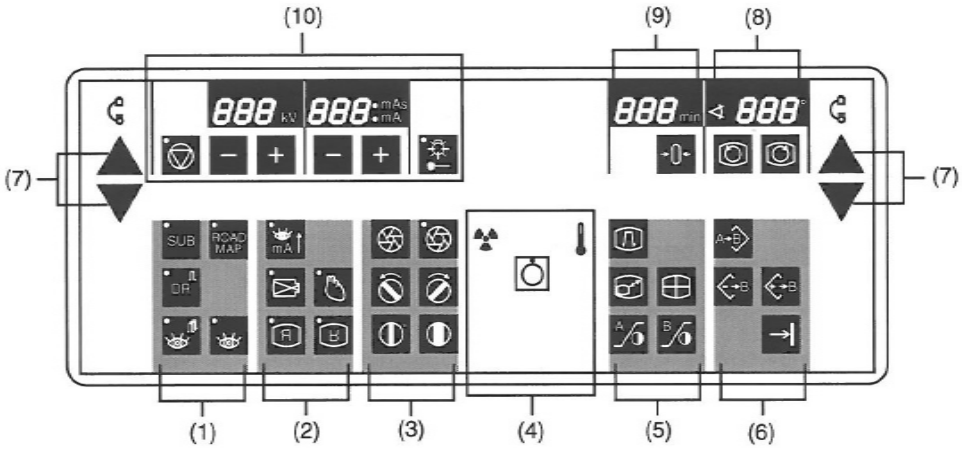

(1) Function modes selection
(2) High efficiency mode selector, parameter adjustment and image-inverting keys.
(3) Collimator adjustment
(4) Radiation indicator, power switch and X-ray generator temperature.
(5) Image post processing
(6) Image selection and storage
(7) Vertical displacement of the C-arm
(8) Image rotation
(9) Exposition time
(10) Scopy and monobloc tube laser tracker selection parameters

C. INCLINATIONS AND SOURCE POSITION CALCULATIONS

Detector tilt angle θ and ϕ calculations

Using the pairs of ball bearings that are parallel to the Z^w axis (Figure 8-1), the converging point, P_θ (explanation below), can be found.

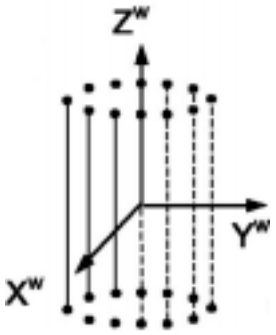

Figure 8-1 Illustration of balls and corresponding lines for detector tilt calculation.

"CONVERGING POINT" CONCEPT EXPLANATION:

The concept of the converging point is used to simplify the explanation of the complex geometry. As seen in Figure 8-2, the X-ray source (P_S) and two ball bearings (P_{BB1} and P_{BB2}) define a plane call divergent plane (D_1). The line L_1 is formed by the intersection D_1 and the detector plane *I*.

When the lines connecting a pair of ball bearings are parallel, as it happens in our particular case, the intersection of the divergent planes (D_i) forms one line (L_d). The intersection of all lines (L_i) is denoted by the converging point (P_C). It can also be defined as the intersection point of L_d and the detector plane *I*.

Converging point always exists except for the case where the axis of divergent planes is parallel to the detector plane.

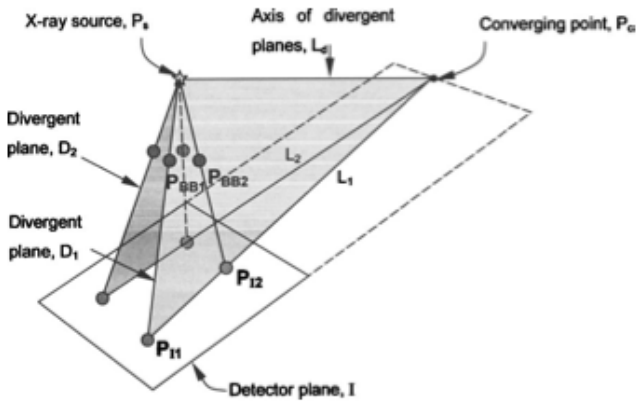

Figure 8-2 Illustration of the elements that define the calculation of the converging point. In this case, lines that connect both pairs of ball bearings are parallel and form the axis of divergent planes.

The converging point P_θ is the one formed due to the detector angle θ. P_θ does not exist when θ is zero regardless of ϕ as shown in Figure 8-3.

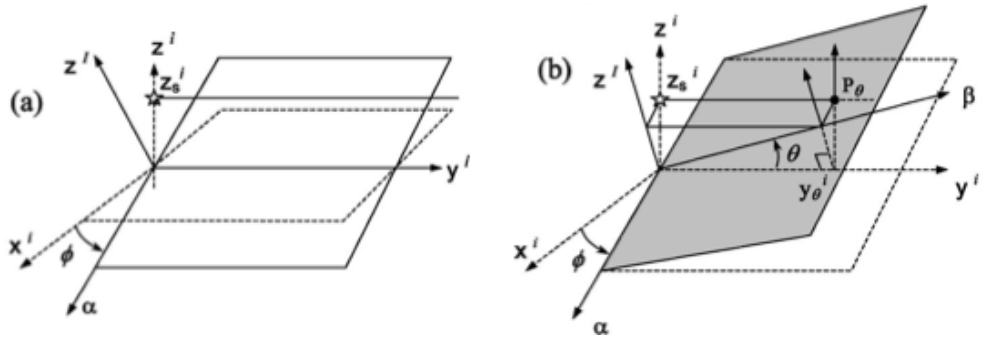

Figure 8-3 Converging point P_θ due to detector angle θ is shown.

The pairs of ball bearings from Figure 8-1 are used to find the axis of divergent plane, which is parallel to Y_i in this case and passes through the source location. P_θ has the following relationship as shown in Figure 8-3:

Being the location of piercing point $P_\theta = (\alpha_\theta, \beta_\theta)$ and found by the intersection of all the lines shown in Figure 8-1 projected in the detector plane,

$$\alpha_\theta = Y_\theta^i \tan(\theta) \tan(\phi)\,,$$

$$\beta_\theta = \frac{Y_\theta^i}{\cos(\theta)} = \frac{Z_S^i cos(\phi)}{\sin(\theta)},$$

and

$$\tan(\phi)\sin(\theta) = \alpha_\theta/\beta_\theta\,.$$

The source position in virtual detector coordinates is the following (as its X-axis component in the virtual detector is zero):

$$P_s^i = \left[0,\, Y_s^i,\, Z_s^i\right].$$

SYSTEM GEOMETRY EXPLANATION

In order to make use of the relationship between virtual detector coordinates and real detector coordinates for its use in the calculation of detector inclinations, $P^I = [X^I,\, Y^I,\, Z^I]^T$ and $P^i = \left[X^i,\, Y^i,\, Z^i\right]^T$ position vector transformation equation is expressed as the following rotation,

$$P^I = R_i^I P^i\,,$$

being the rotation matrix as it follows,

$$R_i^I = \begin{bmatrix} \cos\phi\cos\eta - \sin\theta\sin\phi\sin\ \eta & \cos\theta\sin\eta & -\sin\phi\cos\eta - \sin\theta\cos\phi\sin\ \eta \\ -\cos\phi\sin\eta - \sin\theta\sin\phi\cos\ \eta & \cos\theta\cos\eta & \sin\phi\sin\eta - \sin\theta\cos\phi\cos\ \eta \\ \cos\theta\sin\ \phi & \sin\theta & \cos\theta\cos\phi \end{bmatrix}$$

where ϕ, θ and η are the tilting and rotation of the detector.

For the calculation of inclinations, previously estimated rotation angle must be corrected in the image. After this, equations relating virtual and real detector coordinates and position vector of the source position in virtual detector coordinates give the following equation,

$$Z_S^I = Y_S^i \sin(\theta) + Z_S^i \cos(\theta)\cos(\phi)\,,$$

and relating it with the converging point,

$$Z_S^I = \sin(\theta)\cos(\theta)\,[\beta_\theta + Y_S^i/\cos\,(\theta)]\,.$$

ELLIPSE MODEL EXPLANATION
(Noo *et al* 2000)

The projection formed in cone-beam of the circular pattern of ball bearings corresponds to an ellipse. The equation describing this ellipse is the following:

$$a(u-u_0)^2 + b(v-v_0)^2 + 2c(u-u_0)(v-v_0) = 1\,,$$

where (u_0, v_0) is the center of the ellipse. According to the method proposed by *Noo* the detector angle ϕ can be calculated using the following equations:

$$\sin\phi = -\frac{c_1\zeta_1}{2a_1} - \frac{c_2\zeta_2}{2a_2},$$

$$\zeta_k = Z_S^I \frac{a_k\sqrt{a_k}}{\sqrt{a_k b_k + a_k^2 b_k (Z_S^I)^2 - c_k^2}}\,, \qquad k = 1{,}2$$

where ζ is an intermediate parameter used in ellipse parameter calculation.

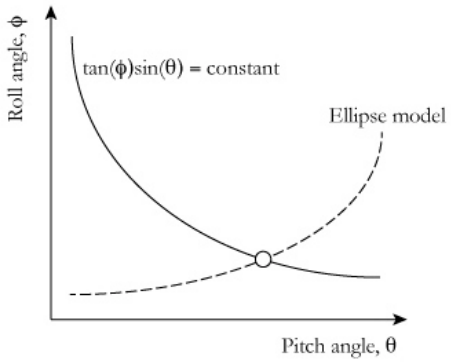

Figure 8-4 Solution of the inclination angles is determined from the intersection of the two curves: the one defined by the ellipse model and the relationship between angles related to the converging point P_θ.

Ellipse model equation:

- From the equations describing ellipse model ϕ is proportional to Z_S^I.
- β_θ is known and $Y_S^i/\cos(\theta)$ is defined by P_ϕ converging point, $Y_S^i/\cos(\theta) = P_0^a$, as seen in Figure 4-6. Therefore, Z_S^I is a function of θ and proportional to it while θ is less than 45º.

As a result, finding the intersection of this equation and the relationship given by the converging point location is simple using a nonlinear root method. The solution is unique when θ is less than 45º.

Calculation of source position $(X_S, Y_S, Z_S)^I$

Firstly, the coordinates related to the virtual detector are calculated:

- X_S^i is zero by definition.
- Y_S^i can be found by the previously equation: $Y_S^i/\cos(\theta) = P_0^a$
- Z_S^i is calculated with the converging point definition $\beta_\theta = Z_S^i \cdot \frac{cos(\phi)}{\sin(\theta)}$. When the θ value is nearly zero, this equation is not stable and the following equation is used: $Z_S^i = (2\ rad\ L_1\ L_2)/[l\ (L_2 - L_1)]$ being *rad* the radius of the circular pattern of ball bearing and *l* the distance between two circular trajectories.

Once $P_s^i = (\mathrm{X_S}, \mathrm{Y_S}, \mathrm{Z_S})^\mathrm{i}$ is known we calculate $P_s^I = (\mathrm{X_S}, \mathrm{Y_S}, \mathrm{Z_S})^\mathrm{I}$ by performing the transformation defined above:

$$P^I = R_i^I P^i$$

9. GLOSSARIUM

- **IORT/RIO: Intraoperative Radiation/Radiación intraoperatoria.**
- **CR: Computed Radiography**
- **CT: Computed Tomography**
- **CBCT: Cone Beam Computed Tomography**
- **DR: Direct Radiography**
- **KeV: Kiloelectron Volt**
- **XRII: X-Ray Image Intensifier**
- **FPD: Flat Panel Detector**
- **RO: Radiation Oncology**
- **FBP: Filtered Backprojection**
- **FDK: Feldkamp, David and Kreis**
- **NMR: Nuclear Magnetic Resonance**
- **PET: Positoron emission tomography**
- **UMCE: Unidad Médica de Cirugía Experimental**
- **HGGM: Hospital General Gregorio Marañón**
- **IDL: Interactive Data Language**
- **FOV: Field of view**
- **SO/SDD: Source to detector distance**
- **UPM: Universidad Politécnica de Madrid**

10.REFERENCES

Abella, M. (2010). Contributions to Image Reconstruction in High-Resolution Multimodality Systems for Preclinical Applications. Unidad de Medicina y Cirugía Experimental. Hospital General Universitario Gregorio Marañón. M. Desco and J. J. Vaquero. Madrid, Universidad Politécnica de Madrid.

Abella, M., J. J. Vaquero, A. Sisniega, J. Pascau, A. Udías, V. García, I. Vidal and M. Desco (2012). "Software Architecture for Multi-Bed FDK-based Reconstruction in X-ray CT Scanners." Computer methods and programs in biomedicine 107(2): 218-232.

Beutel, J., H. L. Kundel and R. L. Van Metter (2000). "Handbook of Medical Imaging." 1.

Cho, Y., D. J. Moseley, J. H. Siewerdsen and D. A. Jaffray (2005). "Accurate technique for complete geometric calibration of cone-beam computed tomography systems." Med. Phys. 32(4): 968-983.

Daly, M. J., S. J. H, C. Y. B, J. D. A and I. J. C (2008). "Geometric calibration of a mobile C-arm for intraoperative cone-beam CT." Medical Physics 35(5): 14.

Fahrig, R. and D. Holdsworth (2000). "Three-dimensional computed tomographic reconstruction using a C-arm mounted XRII: Image-based correction of gantry motion nonidealities." Medical Physics 27: 8.

Hesse, B. M., L. Spies and B. A. Groh (1998). "Tomotherapeutic portal imaging for radiation treatment verification." Phys. Med. Biol. 43: 9.

Jaffray, C. A., J. H. Siewerdsen, J. W. Wong and A. A. Martinez (2002). "Flat-panel cone-beam computed tomography for image-guided radiation therapy." Int. J Radiat. Oncol., Biol., Phys. 53: 12.

Jan, J. (2006). "Planar X-Ray Imaging." Medical Image Processing, Reconstruction and Restoration Concepts and Methods: 15.

Kak, A. C., Slaney, Malcolm (1988). Principles of Computerized Tomographic Imaging.

Körner, M., C. H. Weber, W. S, P. K, R. M. F and T. M (2007). "Advances in Digital Radiography: Physical Principles and System Overview." RadioGraphics 27: 7.

Massarut, S., G. Baldassare, B. Belleti and S. Recanello (2008). "Targeted intraoperative radiotherapy impairs the stimulation of breast cancer cell proliferation and invasion caused by surgical wounding." Clin. Cancer Res. 14(5): 7.

Navab, A., A. Bani-Hashemi and M. Mitshke (2003). "Dynamic geometric calibration for 3-D cerebral angiography." Proc. SPIE Medical Imaging 5030: 10.

Noo, F., R. Clackdoyle, C. Mennessier, T. A. White and T. J. Roney (2000). "An analytic method based on identification of ellipse parameters for scanner calibration in conebeam tomography." Phys. Med. Biol. 45: 3489-3508.

Rougee, A., C. Picard, C. Ponchut and Y. Trousset (1993). "Geometrical calibration of x-ray-imaging chains for 3-dimensional reconstruction." Comput. Med. Imaging Graph. 17: 295-300.

Sun, Y., Y. Hou, F. Y. Zhao and J. H. Hu (2006). "A calibration method for misaligned scanner geometry in cone-beam computed tomography." NDT&E Int. 39(6): 499-513.

Vendantham, S., A. Karellas and S. Suryanarayanan (2000). "Full breast digital mammography with an amorphous silicon-based flat panel detector: Physical characteristics of a clinical prototype." Medical Physics 27(3): 9.

von Smekal, L., M. Kachelriess, E. Stepina and W. Kalender (2004). "Geometric misalignment and calibration in cone-beam tomography." Med. Phys. 31: 3242-3266

Xue, P. and D. L. Wilson (1998). "Effects of motion blurring in x-ray fluoroscopy." Medical Physics 25(587): 13.